

# The reaction $np \rightarrow pp\pi^-$ from threshold up to 570 MeV

M. Daum<sup>2</sup>, M. Finger<sup>3,4</sup>, M. Finger, Jr.<sup>4</sup>, J. Franz<sup>1</sup>, F.H. Heinsius<sup>1</sup>, A. Janata<sup>4</sup>, K. Königsmann<sup>1</sup>, H. Lacker<sup>\*1</sup>, F. Lehar<sup>5</sup>, H. Schmitt<sup>1</sup>, W. Schweiger<sup>1</sup>, P. Sereni<sup>1</sup>, and M. Slunečka<sup>3,4</sup>

<sup>1</sup> Fakultät für Physik der Universität Freiburg, D-79104 Freiburg, Fed. Rep. Germany

<sup>2</sup> PSI, Paul-Scherrer-Institut, CH-5232 Villigen, Switzerland

<sup>3</sup> Universita Karlova, MFF, V Holešovičkách 2, 18000 Praha 8, Czech Republic

<sup>4</sup> Joint Institute for Nuclear Research, LNP, Ru-141980 Dubna, Moscow Region, Russia

<sup>5</sup> DAPNIA/SPP, CEA/Saclay, F-91191 Gif-sur-Yvette CEDEX, France

**Abstract.** The reaction  $np \rightarrow pp\pi^-$  has been studied in a kinematically complete measurement with a large acceptance time-of-flight spectrometer for incident neutron energies between threshold and 570 MeV. The proton-proton invariant mass distributions show a strong enhancement due to the  $pp(^1S_0)$  final state interaction. A large anisotropy was found in the pion angular distributions in contrast to the reaction  $pp \rightarrow pp\pi^0$ . At small energies, a large forward/backward asymmetry has been observed. From the measured integrated cross section  $\sigma(np \rightarrow pp\pi^-)$ , the isoscalar cross section  $\sigma_{01}$  has been extracted. Its energy dependence indicates that mainly partial waves with  $Sp$  final states contribute.

Note: Due to a coding error, the differential cross sections  $d\sigma/dM_{pp}$  as shown in Fig. 9 are too small by a factor of two, and in Table 3 the differential cross sections  $d\sigma/d\Omega_\pi^*$  are too large by a factor of  $10/2\pi$ . The integrated cross sections and all conclusions remain unchanged. A corresponding erratum has been submitted and accepted by European Physics Journal.

## 1 Introduction

Pion production is the basic inelastic process in nucleon-nucleon interaction. Triggered by the high precision data for proton-proton induced reactions [1], a renewed interest arose within the last decade. It has been found that the existing theoretical description [2] at that time underestimated the near-threshold cross section data for  $pp \rightarrow d\pi^+$  by a factor of 1.8 [3] and for  $pp \rightarrow pp\pi^0$  even by a factor of 5 [4]. Refinements by including the  $\Delta$  isobar and the introduction of an energy dependence in the  $s$ -wave rescattering term provided an enhancement of the cross section prediction by about a factor of 2 [5]. Heavy-meson-exchanges [6] and the 'offshell' behaviour of the  $\pi N$  amplitude in the rescattering diagram [7] were discussed as possible mechanisms and were both able to explain the discrepancy.

In recent years, calculations with microscopic models for the  $NN$  and  $\pi N$  interactions based on meson exchange were developed by groups in Jülich [8,9,10,11] and Osaka [12,13]. At present, these are the only models considering all single pion production channels including higher partial waves.

In addition, first calculations in chiral perturbation theory were performed for neutral pion production, [14,15,16,17] and charged pion production [18]. For neutral pion production also one-loop diagrams in the formalism of heavy baryon chiral perturbation theory were calculated [19,20,

21]. Recently, also higher partial waves were calculated in the framework of chiral perturbation theory [22]. It was also shown, that the information that can be deduced from pion production in nucleon-nucleon collisions is relevant for constraining three nucleon forces. In the context of this presentation it is important that the relevant operator structure that allows this connection contributes to the reaction  $np \rightarrow pp\pi^-$  as well.

To pin down the different production mechanisms, high precision data from different pion production reactions are needed. This paper addresses an improvement of the data quality for charged pion production in neutron-proton collisions in order to achieve a better knowledge on the isoscalar cross section  $\sigma_{01}$ .

## 2 Pion production in np collisions

Under the assumption of isospin invariance, all single pion production reactions in nucleon-nucleon collisions into a three body final state can be decomposed into three partial cross sections  $\sigma_{I_i I_f}$ , where  $I_i$  and  $I_f$  denote the isospin of the two-nucleon system in the initial and final state, respectively [23] (see Tab. 1). At medium energies, the cross sections  $\sigma_{11}$  and  $\sigma_{10}$  are dominated by the excitation of the intermediate  $\Delta_{33}$  resonance and are well-measured even close to threshold [1, 24, 25, 26, 27]. In contrast, the isoscalar cross section  $\sigma_{01}$ , which has to be extracted from pion production data in neutron-proton and proton-proton collisions (see Sec. 2.1), is not well-known. Due to isospin conservation, the  $N\Delta$  intermediate state is not accessible from an  $I = 0$  initial state and therefore  $\sigma_{01}$  is expected to be small if resonance production dominates.

### 2.1 Determination of $\sigma_{01}$

The cross section  $\sigma_{01}$  can be extracted from  $np \rightarrow NN\pi^\pm$  data by measuring

$$\sigma_{np \rightarrow NN\pi^\pm} = \frac{1}{2}(\sigma_{11} + \sigma_{01}) \quad (1)$$

from which

$$\sigma_{01} = 2 \cdot \sigma_{np \rightarrow NN\pi^\pm} - \sigma_{11} \quad (2)$$

is obtained. The  $\sigma_{11}$  cross section in the intermediate energy range is well-known from  $pp \rightarrow pp\pi^0$  measurements. However, the situation for  $\sigma_{01}$  was not clear in the past. Several experiments reported significant  $\sigma_{01}$  values below 600 MeV [28, 29, 30, 31, 32], while others found small or even negligible  $\sigma_{01}$  contributions for energies up to 750 MeV [33, 34, 35]. A partial wave analysis of Arndt and Verwest [36] gave no significant  $\sigma_{01}$  contribution below 1 GeV while Bystricky et al. [37] found small, but non-negligible values in a similar analysis. This unsatisfactory finding may be addressed to large experimental uncertainties and inconsistencies in both, the pp and the np data at that time. The determination of  $\sigma_{01}$  from several former np cross section measurements suffered from averaging the results over a large neutron beam energy range [28, 30, 38]. The  $pp \rightarrow pp\pi^0$  data have been remarkably improved during the last decade. Hence, the energy dependence of  $\sigma_{np \rightarrow NN\pi^\pm}$  has to be determined with much higher precision than it was obtained by former experiments in order to extract  $\sigma_{01}$  reliably.

The determination of  $\sigma_{01}$  includes a principal model dependence as (2) only holds in the case of exact isospin invariance. However, due to the different particle masses entering into the reactions  $np \rightarrow pp\pi^-$ ,  $np \rightarrow nn\pi^+$  and  $pp \rightarrow pp\pi^0$ , isospin invariance is only an approximate symmetry. As a consequence, the comparison of the cross sections can not be performed at the same beam energy. Two methods have been discussed in the literature [31, 32] so far which will be denoted in the present discussion as the  $\eta$ - and the  $\sqrt{s}$ -scheme, respectively. In the

Reaction	Decomposition
$pp \rightarrow pp\pi^0$	$\sigma_{11}$
$pp \rightarrow np\pi^+$	$\sigma_{11} + \sigma_{10}$
$pp \rightarrow d\pi^+$	$\sigma_{10}(d)$
$nn \rightarrow nn\pi^0$	$\sigma_{11}$
$nn \rightarrow np\pi^-$	$\sigma_{11} + \sigma_{10}$
$nn \rightarrow d\pi^-$	$\sigma_{10}(d)$
$np \rightarrow nn\pi^+$	$\frac{1}{2}(\sigma_{11} + \sigma_{01})$
$np \rightarrow pp\pi^-$	$\frac{1}{2}(\sigma_{11} + \sigma_{01})$
$np \rightarrow np\pi^0$	$\frac{1}{2}(\sigma_{10} + \sigma_{01})$
$np \rightarrow d\pi^0$	$\frac{1}{2}\sigma_{10}(d)$

**Table 1.** Decomposition of pion production cross sections in partial cross sections  $\sigma_{I_i I_f}$ .

$\eta$ -scheme, the subtraction is performed at equal values of  $\eta = p_{\pi, \max}^*/m_{\pi^+}$ , the maximum value of the dimensionless c.m. pion momentum. In the  $\sqrt{s}$ -scheme the two reactions are compared at the same c.m. energy  $\sqrt{s}$ . This corresponds to a resonant production mechanism with a  $\Delta N$  intermediate state. However, near the production threshold, it neglects the different threshold values for the three reactions.

A modification of the  $\sqrt{s}$ -scheme, the  $Q$ -scheme, performs the subtraction at equal excess energies  $Q = \sqrt{s} - \sqrt{s_{\text{thr}}}$  above the c.m. threshold value  $\sqrt{s_{\text{thr}}}$ . In the  $\sqrt{s}$ -scheme the differences in beam energy are  $\Delta T = T_n - T_p = -2.6$  MeV, whereas for the  $\eta$ - and the  $Q$ -scheme, the difference in beam energy is quite similar and reads  $\Delta T \approx +7$  MeV at  $T_n = 350$  MeV and  $\Delta T \approx +4$  MeV at  $T_n = 550$  MeV. Since the cross section rises strongly between threshold and about 700 MeV beam energy, the results on  $\sigma_{01}$  in the  $\sqrt{s}$ -scheme on one hand and in the  $\eta$ - and the  $Q$ -scheme on the other hand differ significantly.

### 2.2 Angular distributions

A different approach to establish the existence of  $\sigma_{01}$  takes advantage of the properties of the pion angular distributions. All single pion production amplitudes with three-body final states can be decomposed in terms of three isospin amplitudes  $M_{I_f I_i}$  [37] which are related to the partial cross sections  $\sigma_{I_i I_f}$  by

$$\sigma_{01} = |-\frac{1}{\sqrt{3}}M_{10}|^2 \quad (3)$$

$$\sigma_{10} = |M_{01}|^2 \quad (4)$$

$$\sigma_{11} = |\frac{1}{\sqrt{2}}M_{11}|^2. \quad (5)$$

The amplitudes for the pion production reactions of interest then become

$$\langle pp\pi^0 | M | pp \rangle = -\langle nn\pi^0 | M | nn \rangle = \frac{1}{\sqrt{2}}M_{11} \quad (6)$$

$$\langle pp\pi^- | M | pn \rangle = -\langle nn\pi^+ | M | np \rangle = \frac{1}{\sqrt{6}}M_{10} + \frac{1}{2}M_{11} \quad (7)$$

$$\langle pp\pi^- | M | np \rangle = -\langle nn\pi^+ | M | pn \rangle = -\frac{1}{\sqrt{6}}M_{10} + \frac{1}{2}M_{11}. \quad (8)$$

Some consequences follow from these relations. Due to the identical particles in the initial state, the pion c.m. angular distribution in the reaction  $pp \rightarrow pp\pi^0$  is forward/backward (f/b)-symmetric. Hence, a f/b-asymmetry observed in the reaction  $np \rightarrow pp\pi^-$  or  $np \rightarrow nn\pi^+$  indicates the presence of  $\sigma_{01}$  caused by an interference between the amplitudes  $M_{10}$  and  $M_{11}$ . The same conclusion holds if differences in the cross sections at the same pion c.m. angle are found for the reactions  $np \rightarrow pp\pi^-$  and  $np \rightarrow nn\pi^+$ .

The differential cross section for the reaction  $np \rightarrow NN\pi^\pm$  can be expanded in terms of powers of  $\cos\theta_\pi^*$  [39]:

$$\frac{d\sigma}{d\Omega} = a_0 \pm a_1 \cdot \cos\theta_\pi^* + a_2 \cdot \cos^2\theta_\pi^* \pm \dots, \quad (9)$$

where the '+' and '-' sign corresponds to the charge of the pion. Assuming that pion orbital angular momenta  $\ell > 1$  can be neglected, the expansion is truncated after the quadratic term. A f/b-asymmetry in the reaction  $np \rightarrow NN\pi^\pm$  is then described by a non-vanishing linear coefficient  $a_1$ . Most experiments measuring the reactions  $np \rightarrow NN\pi^\pm$  found significant linear cosine terms for energies well below 600 MeV [28,39] and small or vanishing values above 600 MeV [33,38,30]. No significant f/b-asymmetry was reported by Bachman et al. [40] at 443 MeV.

Historically, pion angular distributions in proton-proton reactions were parametrized by

$$\frac{d\sigma}{d\Omega} = C \cdot \left( \frac{1}{3} + b \cdot \cos^2\theta_\pi^* \right) \quad (10)$$

where  $b$  is called the anisotropy parameter. To include an angular asymmetry for the reaction  $np \rightarrow NN\pi^\pm$ , one may add a  $\cos\theta_\pi^*$  term resulting in

$$\frac{d\sigma}{d\Omega} = C \cdot \left( \frac{1}{3} + a \cdot \cos\theta_\pi^* + b \cdot \cos^2\theta_\pi^* \right). \quad (11)$$

This parametrization is still appropriate for comparison with older data. Below 600 MeV, most experiments found anisotropy parameters  $b$  for the reaction  $np \rightarrow NN\pi^\pm$  which were significantly larger than those of the reaction  $pp \rightarrow pp\pi^0$  [28,31,39,40] indicating the presence of the  $\sigma_{01}$  cross section in  $np \rightarrow NN\pi^\pm$ . Nevertheless, no conclusion concerning the energy dependence of  $b_{np \rightarrow NN\pi^\pm}$  can be drawn from the existing data sets (see Sect. 5.2), since they are not fully compatible. Moreover, some experiments [31,39] were restricted by acceptance cuts and could extract the parameters only in a model-dependent way.

### 2.3 Partial waves

A helpful tool for the understanding of the production mechanism is provided by a partial wave decomposition of the scattering matrix. In a usual coupling scheme, the partial wave is written as  $^{2S+1}L_J \rightarrow ^{2S'+1}L'_J \ell_J$ , where  $S$  is

the total spin,  $L$  the orbital angular momentum and  $J$  the total angular momentum of the two nucleons in the initial state, while  $S'$ ,  $L'$  and  $J'$  give the corresponding angular momenta in the final state. The orbital angular momentum of the pion with respect to the final state di-nucleon system is denoted by  $\ell$ . The conservation of angular momentum, isospin and parity and the consideration of the Pauli principle for the di-nucleon system in the initial and final state lead to a remarkable reduction of possible partial waves. In particular, in the reactions  $np \rightarrow NN\pi^\pm$  and  $pp \rightarrow pp\pi^0$ , partial waves with Ss final states can only contribute to  $\sigma_{11}$  and partial waves with Sp final states only to  $\sigma_{01}$ . There is only one possible Ss partial wave,  $^3P_0 \rightarrow ^1S_0s_0$ , whereas there are two possibilities that lead to Sp partial waves,  $^3D_1 \rightarrow ^1S_0p_1$  and  $^3S_1 \rightarrow ^1S_0p_1$ . Each partial wave shows a characteristic angular dependence as a function of  $\theta_\pi^*$ , which is constant in the case of  $^3P_0 \rightarrow ^1S_0s_0$  and  $^3S_1 \rightarrow ^1S_0p_1$  while it is described by  $\frac{1}{3} + \cos^2\theta_\pi^*$  for  $^3D_1 \rightarrow ^1S_0p_1$ . A further interesting feature of partial waves is the expected  $\eta$  dependence of their excitation function. If the pp final state interaction can be neglected, as in the case for pp P-waves, an  $\eta$  dependence  $\propto \eta^{2 \cdot (L' + \ell + 2)}$  is expected [41]. In contrast, for pp S-waves the final state interaction plays an important role. In this case, an excitation function of the form  $\propto \eta^{2 \cdot (\ell + 1)}$  is expected [41]. However, in the reaction  $pp \rightarrow pp\pi^0$  close to threshold, where only the partial wave  $^3P_0 \rightarrow ^1S_0s_0$  contributes, a clear deviation from the naive  $\eta^2$ -dependence was observed [1].

### 2.4 Recent developments

Considerable improvement has been achieved during the last decade with new medium-energy-accelerators which provided secondary neutron beams of high intensity and high polarisation as well. Below the two-pion production threshold, single spin observables in the reaction  $np \rightarrow pp\pi^-$  have been measured at TRIUMF at 443 MeV [40] and at SATURNE at 572 MeV [42]. Exclusive experiments at TRIUMF with proton beams at energies of 353, 403 and 440 MeV incident on a deuterium target were dedicated to investigate the  $pp(^1S_0)$  final state [43,44]. They revealed the significance of the  $\sigma_{01}$  cross section in that particular phase space configuration by a subsequent partial wave analysis considering the partial waves  $^3S_1 \rightarrow ^1S_0p_1$  and  $^3D_1 \rightarrow ^1S_0p_1$  for the  $I = 0$  and  $^3P_0 \rightarrow ^1S_0s_0$  for the  $I = 1$  initial state [44]. At 440 MeV, even a small contribution from pion d-waves  $^3P_2 \rightarrow ^1S_0d_2$  and  $^3F_2 \rightarrow ^1S_0d_2$  was reported.

Despite of this progress, the data of pion production in neutron-proton collisions are still lacking precise measurements of differential and integrated cross sections. In this paper, we report on a kinematically complete measurement of the reaction  $np \rightarrow pp\pi^-$  using a polarised neutron beam. Here, we deal only with spin averaged results while spin dependent observables will be presented in a forthcoming publication. Details of the analysis can be found in [45].

### 3 Experiment

#### 3.1 Neutron Beam

We used the polarised neutron beam facility NA2 at Paul-Scherrer-Institut (PSI) which is described in detail in Ref. [46]. Vertically polarised protons from an atomic beam source were accelerated in the cyclotron to an energy of 590 MeV. The beam polarisation vector was then rotated from vertical into longitudinal direction and was reversed every second at the source. Longitudinally polarised neutrons were produced in the reaction  $^{12}\text{C}(p, n)X$  on a 12 cm thick carbon target [46, 47]. Neutrons emitted at  $0^\circ$  with respect to the proton beam axis were selected by means of a collimator of 2 m length. The neutron beam was stabilized on its axis using a feed back system which kept the proton beam at the center of the neutron production target within 0.1 mm [48]. Remaining beam protons and secondary charged particles were deflected by a dipole magnet. A lead filter reduced the  $\gamma$ -contamination in the beam, originating mainly from the decay of neutral pions which were produced in the neutron production target. Spin rotating magnets allowed to choose any neutron polarisation direction. All results presented in this paper were achieved by averaging the data for the two beam polarisation states for a transversely polarised neutron beam.

The time structure of the PSI proton beam consists of bunches of 0.84 ns width (FWHM) with a bunch frequency of 50.63 MHz. The neutrons show a continuous energy distribution with a quasi-elastic peak at about 530 MeV and a broad continuum at lower energies resulting mainly from pion production and  $\Delta$  excitation [49]. For a typical proton beam current of 10  $\mu\text{A}$  and a beam collimator opening of 9 mm diameter, a neutron beam with a typical flux of several  $10^7$  n/s was obtained. The beam was 4 cm in diameter (FWHM) at 20 m downstream of the neutron production target.

Two monitors, described in [46], were used to check the neutron beam properties during data taking and in the offline analysis. Monitor I was placed immediately behind the neutron beam pipe window in the NA2 area and allowed a relative measurement of the neutron beam intensity using the reactions  $\text{H}^1(n, p)n$  and  $\text{C}(n, p)X$  in a Polyethylene target. It consisted of three scintillator counters M1, M2 and M3 with the Polyethylene target sandwiched between M1 and M2. The counting rate  $\overline{M1} \cdot M2 \cdot M3$  served as a measure of the neutron beam intensity. Monitor II was placed 2 m behind the experimental set-up. It measured the beam position and the beam profile using a scintillator hodoscope. The beam polarisation in horizontal and transverse direction was monitored by two-arm polarimeters. For the two different polarisation states at the source (flipped and non-flipped), the neutron beam intensities, positions and polarisations were found to be equal within the statistical errors.

#### 3.2 Experimental set-up

For the kinematically complete measurement of the reaction  $np \rightarrow pp\pi^-$ , a time-of-flight (TOF) spectrometer

with a large geometrical acceptance was used. In the reaction  $np \rightarrow pp\pi^-$ , both protons are emitted within the angular range  $0^\circ < \theta_p < 45^\circ$  in the laboratory system for neutron kinetic energies below 570 MeV. The pion emission angle is not constrained for any neutron energy above 313 MeV. The experiment relied on the determination of the energy for each incident neutron provided by a TOF measurement and the reconstruction of the emission angles and velocities of at least two of the three charged particles in the final state. The experimental set-up (Fig. 1) consisted of a liquid hydrogen target, two sets of drift chambers (DC8, BD6) as tracking devices, a segmented trigger hodoscope and a large area TOF wall.

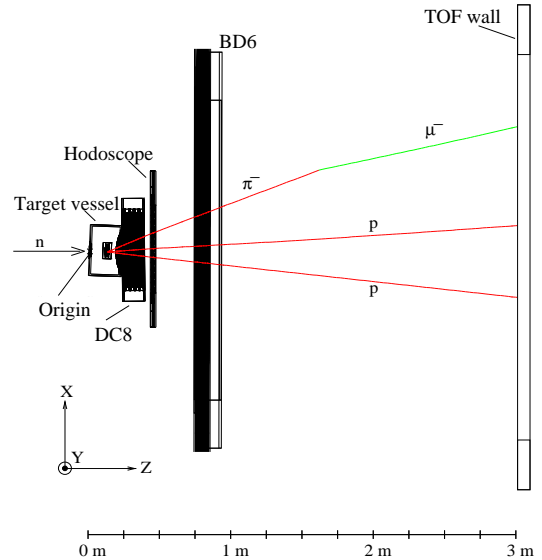


Fig. 1. Top view of the detector.

The lens-shaped target cell with walls consisting of a 125  $\mu\text{m}$  thick Kapton layer was filled with liquid hydrogen and placed 20.03 m downstream of the neutron production target. It was 9.3 cm in diameter and 3.15 cm thick at central incidence and surrounded by several layers of superinsulation with a total thickness of 340  $\mu\text{m}$ . The target cell was placed inside a vacuum vessel with an entrance and exit window of 10 cm and 30.8 cm diameter, respectively. Both were sealed by titanium sheets of 25  $\mu\text{m}$  (entrance) and 50  $\mu\text{m}$  (exit) thickness.

The drift chamber DC8 with an active area of  $56 \times 56 \text{ cm}^2$  was placed immediately behind the target vessel. It consisted of eight planes with alternating wire orientations in vertical (Y) and horizontal (X) direction. Each plane contained 14 cells of 4 cm width equipped with pairs of signal wires with a wire spacing of 0.42 mm in order to avoid left-right ambiguities for a single track crossing the drift cell. The large drift chamber stack BD6 consisted of 6 planes with an active area of  $214 \text{ cm}(X) \times 114 \text{ cm}(Y)$  and with wire orientations UYVUYV where U and V denote directions of  $\pm 30^\circ$  with respect to the Y direction. Each

drift cell had a width of 2 cm and was equipped with one signal wire.

For both drift chambers, a gas mixture of 67.8 % Argon, 29.5 % Isobutane and 2.7 % Methylal was used. The average detection efficiency per plane extracted from one-track events (mainly protons) was found to be 97% for DC8 and 95% for BD6. The spatial resolution for the DC8 planes was determined to be  $\sigma = 0.2$  mm for track angles of  $0^\circ$  with respect to the neutron beam axis increasing up to 0.5 mm at  $40^\circ$  in agreement with former findings for the same chamber type [50].

The trigger hodoscope which was placed immediately behind the DC8 had an active area of  $65 \times 65 \text{ cm}^2$  and consisted of two planes with horizontal(h) and vertical(v) scintillator slabs. Both planes were built up by twelve scintillator slabs with an area of  $65 \times 5 \text{ cm}^2$  and a thickness of 0.3 cm. Each slab was instrumented from both sides with HAMAMATSU R1450 photomultiplier tubes. In the central part of both planes, two scintillators ( $30 \times 5 \times 0.3 \text{ cm}^3$ ), instrumented with only one photomultiplier tube, were placed in order to leave a quadratic gap of  $5 \times 5 \text{ cm}^2$  for the neutron beam. By this gap, generation of a large background rate in the detector by beam interactions inside the hodoscope was avoided. For a fast timing BICRON BC404 scintillator material was chosen in conjunction with BC800 as lightguide material in order to minimize light losses in the UV range.

Three meters downstream from the hydrogen target cell a large scintillator TOF wall with an area of  $300 \times 290 \text{ cm}^2$  was installed. The wall consisted of two groups of seven BC412 scintillator bars with dimensions of  $300 \times 20 \times 8 \text{ cm}^3$  instrumented on both sides with Philips XP2040 photomultiplier tubes. The bars and photomultipliers had been already used in the LEAR experiment PS199 [51]. The two groups were separated by two smaller BC408 scintillator bars with dimensions of  $100 \times 10 \times 10 \text{ cm}^3$  viewed from the outer side by Philips XP2020 photomultiplier tubes. They were placed to leave a gap of  $10 \times 10 \text{ cm}^2$  in the centre of the TOF wall for the neutron beam.

### 3.3 Electronics and data acquisition

The electronics for all scintillator detectors had been already successfully operated in the LEAR experiment PS199 [51] and the PSI experiments on elastic  $np$  scattering [52]. Compact CAMAC-modules, constructed by the University of Geneva, with constant-fraction discriminators and mean-timers (DPNC 982) provided output signals for ADC and TDC measurements as well as for trigger building. The TDC measurement was performed with time-to-charge converter (TQC) modules, constructed by the University of Geneva, and LeCroy 4300 ADC CAMAC-modules for charge digitization, resulting in a time resolution of 50 ps. For the ADC measurement, LeCroy 4300 CAMAC-modules were used. A dedicated ADC and TDC channel readout by the data acquisition software according to the fired scintillators was realized using LeCroy 4448 coincidence register modules. The number of hits for each scintillator plane was determined by a LeCroy

4532 majority logic unit (MALU) generating output signals in case of at least one hit ( $ORO$ ) and at least two hits ( $MDO$ ). A traversing of the hodoscope by at least two charged particles was indicated by the coincidence signal  $TCP = (ORO_h \wedge MDO_v) \vee (MDO_h \wedge ORO_v)$ . The subscripts h, v refer to horizontal and vertical orientation, respectively.

Both drift chambers were instrumented with electronics cards, developed by the University of Freiburg, performing pre- and main-amplification as well as discrimination of the drift chamber signals [53]. Drift time measurement was provided by LeCroy 1879 FASTBUS modules with a TDC resolution of 2 ns. Moreover, the hit multiplicity for each DC8 plane was determined using multiplicity cards, constructed at the University of Freiburg and successfully operated at the LEAR experiment PS202 [54]. The output signals of these cards were used in the second level trigger stage.

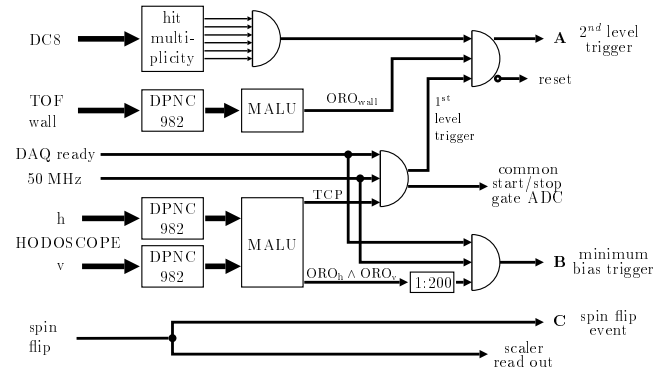


Fig. 2. Overview of the trigger electronics.

Three different types of triggers were used in the experiment. A simplified scheme of the trigger electronics is shown in Fig. 2.

A) The main trigger consisted of two levels and intended to select events of the reaction  $np \rightarrow pp\pi^-$  by requiring a charged multiplicity of at least two. The first level trigger was built by a coincidence of i) the 50.63 MHz radio frequency signal of the accelerator (50 MHz), ii) the  $TCP$  coincidence signal and iii) a computer-ready signal from the data acquisition system. The 50 MHz signal indicated the arrival time of the proton bunch at the neutron production target modulo 19.75 ns which is the cyclotron repetition time. It determined the timing of the first level trigger which served as a common stop signal for the drift chamber FASTBUS TDCs as well as a common start signal for the hodoscope and TOF wall scintillator TQCs providing the times  $TOF_{hodo}$  and  $TOF_{wall}$ . Both times are measured modulo 19.75 ns. They include the time-of-flight from the neutron production target to the liquid hydrogen target ( $TOF_1$ ) and in addition the short time-of-flight to the hodoscope ( $TOF_2$ ) and respectively to the

TOF-wall ( $TOF_2 + TOF_3$ ), (see Fig. 3):

$$TOF_{\text{hodo}} = TOF_1 + TOF_2 + i \cdot 19.75 \text{ ns} \quad (12)$$

$$TOF_{\text{wall}} = TOF_1 + TOF_2 + TOF_3 + i \cdot 19.75 \text{ ns} \quad (13)$$

where  $i = 0, 1, \dots$

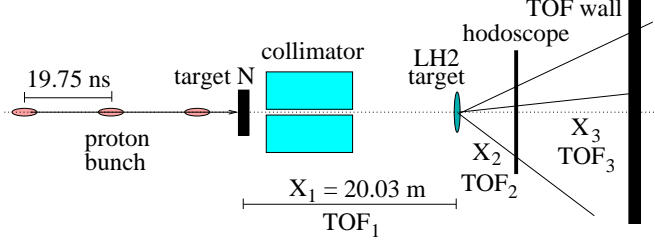


**Fig. 3.** Principle of the time-of-flight measurements.

The second level trigger required at least one hit in the TOF wall ( $ORO_{\text{wall}}$ ) and at least one hit in each DC8 plane. The latter condition suppressed a large part of events originating from beam interactions in the hodoscope or the DC8 chamber. If the second level trigger condition was not fulfilled, a fast-clear signal was sent to all modules.

B) A minimum bias trigger which required, at the first level, a minimum charged multiplicity of one in the hodoscope and no further requirements at the second level was accepted with a prescaling factor of 1:200 corresponding to about 20% of the total trigger rate. These events were mainly elastic  $np$  scattering events giving by far the largest contribution to the total  $np$  cross section in this energy range.

C) A pseudo-event trigger signal was generated at the end of each one-second-period and all main and minimum bias trigger signals were rejected during a 10 ms INHIBIT signal. During this time interval the proton beam polarisation at the beam source was reversed and scaler registers were read out and reset.

The data acquisition and readout was controlled by a STARBURST ACC2180 front end computer which buffered events and sent them in data packages to a VAX4090 workstation where they were written to tape. Typical triggered event rates were of the order of 260 events per second with an average event length of 250 Bytes. The life time of the data acquisition system was about 30 – 40%. For the determination of the spin averaged results, about  $6 \cdot 10^7$  events with transversely polarised neutrons were recorded. This includes also dedicated calibration runs. About  $2 \cdot 10^7$  triggers with transversely and longitudinally polarised neutrons were taken with an empty target cell in order to study background contributions originating from the target surroundings.

## 4 Event reconstruction

The reconstruction of the reaction  $np \rightarrow pp\pi^-$  relied on the energy determination of each incident neutron by a

category	measured observables
C1	2-prong + 2 velocities
C2	3-prong + 1 velocity
C3	3-prong + 2 velocities
C4	3-prong + 3 velocities

**Table 2.** Fit categories and measured observables.

time-of-flight measurement and the measurement of a sufficient set of track parameters and velocities for the emitted particles. For a given neutron energy, nine kinematical observables, *e.g.*, the momentum vectors of the three particles in the final state, describe the kinematical state completely. Due to energy-momentum conservation, it is sufficient to measure five of those. Events of the reaction  $np \rightarrow pp\pi^-$  were reconstructed using a kinematical fit of at least six measured kinematical observables, and thereby separated from background. As a consequence, the reaction  $np \rightarrow pp\pi^-$  could only be reconstructed from 2- and 3-prong events but not from 1-prong events. However, 1-prong events from the minimum bias trigger sample were used to reconstruct elastic  $np$  scattering events. In the case of 2-prong events, the velocity for both tracks had to be measured in order to perform a kinematical fit. For 3-prong events, the six track angles, in principle, were already sufficient. Nevertheless, at least one particle velocity was required in order to determine the neutron time-of-flight (see Sec. 4.3). The particle velocities were given by two different types of time measurements. In general, they were determined from the time-of-flight  $TOF_3$  between the hodoscope and the TOF wall. In some cases, they were given by a determination of the time-of-flight  $TOF_2$  between the liquid hydrogen target and the hodoscope (see Sec. 4.4).

If one of the measured tracks could be associated to a pion or two measured tracks could be assigned to protons, the final state was completely fixed. This association was performed using kinematical arguments. Otherwise, up to three configurations were possible. In this case, the configuration with the best  $\chi^2$  defined the particle-to-track association.

According to the number of measured velocities in 2- and 3-prong events, four categories were defined for the kinematical fit. Their classification,  $C\nu$ , corresponding to the number of degrees of freedom  $\nu$ , is shown in Tab. 2.

### 4.1 Track reconstruction

Tracks were searched using the drift chambers BD6 and DC8. In the first stage, three-dimensional track intersection points were reconstructed inside the large drift chamber (BD6) by combining only the positions of the hit wires in the U-, V- and Y-planes. This procedure speeds up the track finding and gives the BD6 intersection point with a sufficient precision of approximately  $\pm 20\text{mm}$  for the subsequent track finding in the DC8.

In the second stage, track intersection points in the BD6 and hits in the first DC8 X- and Y-plane provided esti-

mates for the track parameters. Hits were then searched in the other DC8 planes inside defined corridors. If at least three hits in both, the X and Y projection, could be found, the track candidate was accepted and a straight line was fitted to these DC8 hits. If more than one candidate was found for a given BD6 intersection point, only the candidate with the best confidence level in the track fit was kept. Track candidates which gave no intercept with the liquid hydrogen target cell were rejected from the further analysis.

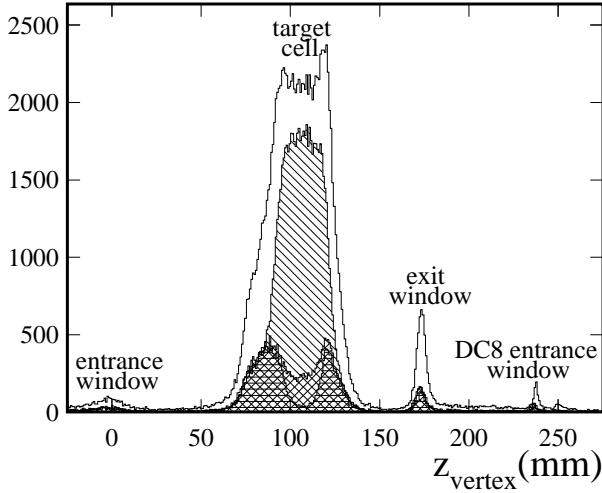


**Fig. 4.** Histogram:  $z$ -positions of reconstructed vertices  $z_{\text{vertex}}$  for 2- and 3-prong events. For the other distributions see Sec. 4.6. Hatched: events with a confidence level  $CL > 0.05$  in the kinematical fit. Cross-hatched: events of ' $p\pi'$ '-type with  $CL > 0.05$ . Horizontal lines: events of ' $p\pi'$ '-type with  $CL > 0.05$  for data with an empty target cell.

Finally, a corridor track search inside the DC8 was performed using only those hits which had not been associated to any track before. For this purpose, it was required that any new track candidate should intersect the liquid hydrogen target cell together with other tracks which had been found already in the second stage. This allowed to find tracks for particles which indeed traversed the DC8 but stopped or, in case of a pion, decayed eventually before reaching the BD6.

For 2-prong events, the vertex was defined as the point of closest approach while for 3-prong events, the vertex of the event was defined as the average of the three 2-track vertices. A typical vertex resolution of the order of 3 mm was found. The  $z$ -position of the reconstructed vertices in the target region (Fig. 4) shows a clear distinction between events originating from the target cell and its surroundings on one hand and events from the target entrance and exit window and the DC8 entrance window on the other hand. For the further analysis a part of background events was rejected by a loose vertex cut of  $70 \text{ mm} < z_{\text{vertex}} < 135 \text{ mm}$ .

## 4.2 Scintillator Information

Scintillators were associated to tracks if i) a track intercept with the fired scintillator was found and ii) the scintillator coordinate, calculated from the time difference between both photomultiplier signals using the measured (effective) scintillator light velocity, corresponded to the track coordinate at the scintillator. Light velocities and spatial resolutions were found to be  $0.47 \cdot c$  and 20 mm ( $\sigma$ ) for the hodoscope and  $0.53 \cdot c$  and 45 mm ( $\sigma$ ) for the TOF wall corresponding to time resolutions of 0.135 ns for the hodoscope scintillators and 0.280 ns for the bars.

Time calibrations for scintillators were performed in several steps. Special runs without lead filters provided a large fraction of high energetic photons in the beam originating from decays of neutral pions in the neutron production target. A part of these photons converted in the  $LH_2$  target and its surroundings into relativistic electron-positron pairs which gave a unique time signal for both times,  $TOF_{\text{hodo}}$  and  $TOF_{\text{wall}}$ . Since the conversion process favours strongly the forward direction, only hodoscope and TOF wall scintillators near the beam line could be calibrated reliably by this method. All bars in the TOF wall far from the beamline were calibrated with events from the minimum bias trigger sample requiring the elastic  $np$  scattering kinematics to be fulfilled. The remaining hodoscope scintillators for a given plane were calibrated by means of the well-calibrated inner scintillators of the other plane using tracks that had traversed both scintillators.

## 4.3 Neutron time-of-flight

The time-of-flight  $TOF_n$  for a neutron with velocity  $\beta_n$  was given by the time  $TOF_{\text{hodo}} - TOF_2$  where  $TOF_2$  was determined from the particle velocity  $\beta_1$  (see Sec. 4.4). For 2- and 3-prong events, the track with the fastest velocity  $\beta_1$  was used for the determination of  $TOF_n$  in order to minimize systematic errors due to the energy loss correction (see Sec. 4.4). In general, the time  $TOF_n$  was ambiguous since the time  $TOF_{\text{hodo}}$  was measured only modulo 19.75 ns. However, due to the reaction threshold of 287 MeV neutron kinetic energy and the chosen distance of 20.03 m between the production target and the liquid hydrogen target,  $TOF_{\text{hodo}}$  was unambiguous for  $np \rightarrow pp\pi^-$  events. Nevertheless, two values for  $TOF_n$  were possible since  $TOF_2$  was slightly different for pions and protons (see Sec. 4.4). The time resolution of  $TOF_n$  was dominated by the width of the incoming proton bunch of 0.355 ns ( $\sigma$ ) resulting in an uncertainty of 3 MeV ( $\sigma$ ) at 287 MeV neutron energy and 9 MeV ( $\sigma$ ) at 570 MeV.

## 4.4 Velocity determination

The velocity  $\beta_1^{\text{meas}}$  along the flight path between the hodoscope and TOF wall scintillator was determined from the time-of-flight  $TOF_3 = TOF_{\text{wall}} - TOF_{\text{hodo}}$ . From  $\beta_1^{\text{meas}}$ , the initial velocity  $\beta_1$  was calculated with an energy loss correction function depending on the track angle and the



track origin inside the liquid hydrogen target using the GEANT 3.21 package [56]. For 2- and 3-prong events, the track origin was defined by the vertex while for 1-prong events it was assumed to be the track intercept with the centre plane of the target cell. The correction also depends on the particle type, and hence two possible velocities,  $\beta_I^p$  and  $\beta_I^\pi$ , have been associated to the track. Protons with  $\beta_I^p < 0.28$  and pions with  $\beta_I^\pi < 0.45$  stopped before reaching the TOF wall. The relative uncertainty  $\delta\beta_I/\beta_I$ , dominated by the time resolution of the TOF wall scintillators, was 3.3% at  $\beta_I = 1$  and 1% at  $\beta_I = 0.3$ .

For several reasons, it was not always possible to determine the velocity  $\beta_I$  for all tracks in a given event: i) several tracks had traversed the same scintillators, ii) the emission angle of a track could lie outside the TOF wall acceptance, iii) a particle stopped or iv) a pion decayed before reaching the TOF wall. This lowered the reconstruction efficiency for 2-prong events substantially. However, the problem was circumvented if  $\beta_I$  was measured for one track, denoted by track 1, and at least  $TOF_{\text{hodo}}$  was available for the other track (track 2). In this case, the time-of-flight for track 2,

$$TOF_2^{21} = TOF_{\text{hodo}}(\text{track 2}) - TOF_n(\text{track 1}), \quad (14)$$

was determined resulting in a velocity measurement, denoted  $\beta_{II}^{\text{meas}}$ . The error due to the time uncertainty of the incoming proton bunch cancels in (14). As a consequence, the uncertainty on  $TOF_2^{21}$  was given by the timing resolution of the hodoscope scintillators traversed by track 2. To reduce the uncertainty on  $\beta_{II}^{\text{meas}}$ , only tracks with  $\beta_{II}^{\text{meas}}$  information in both hodoscope planes were accepted. This resulted in the relative uncertainty  $\delta\beta_{II}/\beta_{II}$  of 8.2% for relativistic particles.

#### 4.5 Particle-to-track association

No dedicated particle identification (PID) was foreseen in the experiment since the detector was designed as a TOF spectrometer. Therefore, the PID was obtained from the kinematical fit procedure. However, if for a given neutron energy the particle velocity superceeded the maximum possible value for a proton in the reaction  $np \rightarrow pp\pi^-$  by three standard deviations, the track was assumed to belong to a pion.

In addition, the combined information from the deposited energy  $E_{\text{DEP}}$  in the TOF wall and the  $\gamma$ -factor  $\gamma_{\text{bar}} = 1/\sqrt{1 - \beta_{I,\text{bar}}^2}$  at the scintillator bar was used in order to exclude the pion hypothesis for certain tracks (Fig. 5). The deposited energy  $E_{\text{DEP}}$  increased with decreasing  $\gamma_{\text{bar}}$  due to the energy loss described by the Bethe-Bloch formula. Pions with  $\gamma_{\text{bar}} < 1.33$  and protons with  $\gamma_{\text{bar}} < 1.1$  stopped and deposited all their kinetic energy  $T_{\text{kin}} = m \cdot (\gamma_{\text{bar}} - 1)$  inside the TOF wall. Clear signals from stopped protons and deuterons are seen. The observed deviation from linearity in the data is caused by a known saturation effect of the meantimer-discriminator module [51]. No significant signal from stopped pions is observed due to several reasons: i) a pion-to-proton ratio of

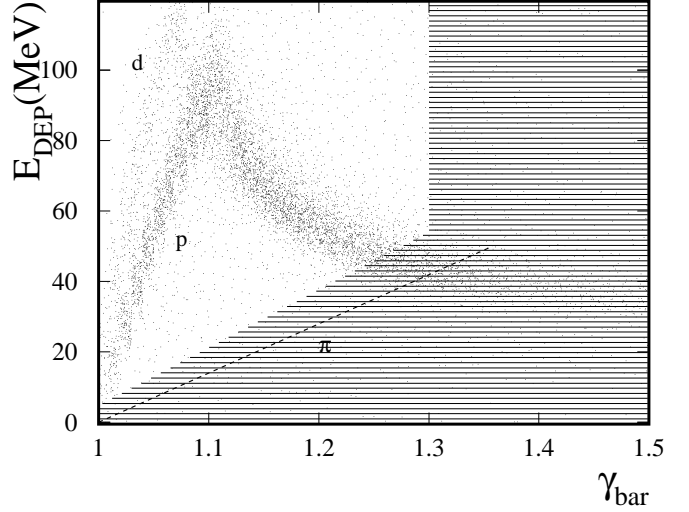


**Fig. 5.** Deposited energy in a TOF wall scintillator bar as a function of  $\gamma_{\text{bar}}$ . Dashed line: expectation for stopped pions. Signals in the white region were considered as originating from protons for the kinematical fit.

only about 1:6 from the reaction  $np \rightarrow pp\pi^-$  is expected within the TOF wall acceptance where most pions have large momenta; ii) the probability for a pion decaying before reaching the TOF wall is more than 50% for  $\gamma < 1.25$ ; iii) pions with  $\gamma < 1.12$  stopped before reaching the TOF wall. For the particle-to-track association, all tracks with entries outside the grey area could not be produced by a pion and hence were considered as originating from a proton.

#### 4.6 Kinematical fit and background rejection

The events were reconstructed using a kinematical fit technique described in Ref. [55]. The incident neutron momentum  $p_n$  was calculated from the neutron velocity  $\beta_n$  where the components  $p_{n,x}$  and  $p_{n,y}$  were assumed to be zero. The set of kinematical variables  $x$  was chosen as  $x = \{p_n; p_1, \theta_1, \phi_1, \dots, p_3, \theta_3, \phi_3\}$  where  $p_i$  denotes the momentum and  $\theta_i$  and  $\phi_i$  the polar and azimuth angle of the emitted particle  $i$ .

Systematic errors in the kinematical fit due to systematic shifts in the measured track parameters and velocities were found to be much smaller than the experimental resolution as indicated by the pull function  $\text{pull}(x) = (x^{\text{meas}} - x^{\text{fit}})/\sqrt{\sigma_{x^{\text{fit}}}^2 - \sigma_{x^{\text{meas}}}^2}$ , where  $x^{\text{meas}}$  and  $x^{\text{fit}}$  denote the measured and fitted values for the observables  $x$ , respectively. The resolutions for the pull functions were found to be between 0.9 and 1.0 with a good agreement between experimental and Monte Carlo data indicating that the experimental errors had been reasonably estimated.

The confidence level distribution  $CL$  shown in Fig. 6 for the data was found to be almost flat with a slight increase towards larger  $CL$  values. The strong enhancement at small  $CL$  values is caused by two kinds of events. About



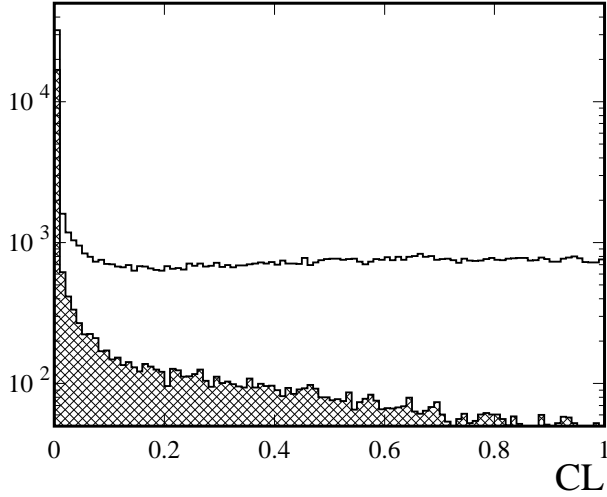


**Fig. 6.** Confidence level distribution for data with full and empty target cell (cross hatched).

half of these events originated from the target surroundings (Fig. 6). The other part are likely  $np \rightarrow pp\pi^-$  events and background reactions of various kinds, *e.g.*,  $np \rightarrow d\gamma$ ,  $np \rightarrow d\pi^0$  and  $np \rightarrow np\pi^0$  where electrons and positrons from the  $\gamma$  conversion in the target surroundings could fake a fast pion. It was shown from Monte Carlo studies that about 8 % of  $np \rightarrow pp\pi^-$  events give an enhancement at small  $CL$  values due to large multiple scattering, hadronic interactions and pion decay. A part of the  $np$  induced background reactions was already reduced by requiring a track intercept with the target cell and the cut on  $z_{\text{vertex}}$  since the electron or positron track from the conversion process rarely matches with the proton or deuteron track. By rejecting all events with  $CL < 0.05$  the reconstruction efficiency for the reaction  $np \rightarrow np\pi^0$  obtained from Monte Carlo was found to be  $6 \cdot 10^{-4}$  resulting in an estimated background contribution of 0.1 %.

Although the cut at  $CL = 0.05$  rejected a large amount of the background reactions in the  $LH_2$  target and the target surroundings, there were still background events from the Kapton walls of the target cell. As can be seen from Fig. 4, these are 2-prong events where one track is associated with a pion and the other with a proton and are denoted ' $p\pi'$ '-events in the following. They are mainly events from the quasi-free reactions on nuclei,  $nn \rightarrow d\pi^-$  and in particular  $nn \rightarrow np\pi^-$ , which have large cross sections due to the contribution of  $\sigma_{10}$ . A part of this background was rejected by the loose vertex cut whereas the main part could not be separated from the reaction  $np \rightarrow pp\pi^-$  neither by the vertex reconstruction nor by the kinematical fit.

For the reaction  $np \rightarrow pp\pi^-$ , events of the ' $p\pi'$ '-type occurred mainly when one proton stopped before reaching the DC8 drift chamber. The minimum momentum in the laboratory system for a final state proton from the reaction  $np \rightarrow pp\pi^-$  decreases with increasing neutron energy. It reads 140 MeV/c at  $T_n = 570$  MeV. It was shown from Monte Carlo studies that protons with momenta less than

190 MeV/c, when emitted from the central position in the target cell, stopped before reaching the hodoscope. At 570 MeV, events of the ' $p\pi'$ '-type from the reaction  $np \rightarrow pp\pi^-$  contribute a few percent. This is confirmed by the data when comparing in Fig. 4 the ' $p\pi'$ '-event distributions for data with full and empty target cell. Hence, it was decided to reject ' $p\pi'$ '-events to reduce a large part of background while keeping most of the signal events. The still remaining background contribution from the target surroundings was of the order 4 % averaged over all neutron energies. It increased with decreasing neutron energy and was about 8 % at 315 MeV.

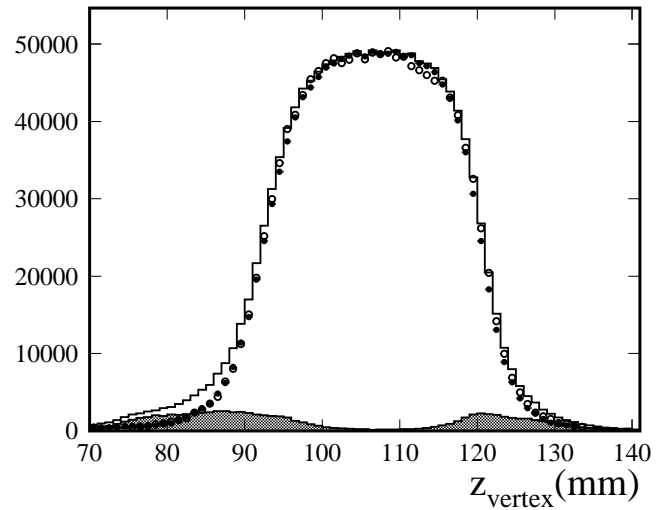


**Fig. 7.** The reconstructed vertex position  $z_{\text{vertex}}$  for 2- and 3-prong events after all cuts for data with full and empty (grey) target cell. The background subtracted distribution is shown as full circles, Monte Carlo data as open circles.

If the pion velocity and one proton velocity were almost of the same magnitude, the kinematical fit could find the wrong permutation. This happened in less than 5 % of the Monte Carlo generated events. However, due to the quite similar kinematical configurations for the correct and wrong reconstructed final state, this combinatorial background has a minor impact on the differential and integrated cross sections.

The reconstructed  $z_{\text{vertex}}$  positions after all cuts are shown in Fig. 7 for the data with full and empty target cell. The background subtracted  $z_{\text{vertex}}$  distribution is in good agreement with the expectation from the Monte Carlo simulation.

#### 4.7 Monte Carlo Simulations

The experiment was simulated using the GEANT 3.21 program package [56] incorporating all relevant materials of the experimental setup. The detector responses were implemented using detector efficiencies, resolutions and

calibrations as they were determined from the experimental data, *e.g.*, the effective light velocities in the scintillators or the time-to-distance relations for the drift chambers. These responses were written in the same data stream format as the experimental data.

Using 3.7 million phase-space distributed Monte-Carlo events, the reconstruction efficiency  $\epsilon_{pp\pi^-}$  for the reaction  $np \rightarrow pp\pi^-$  was determined as a function of the incoming neutron kinetic energy  $T_n$ , the pion c.m. angle  $\theta_\pi^*$  and the proton-proton invariant mass  $M_{pp}$ :

$$\epsilon_{pp\pi^-} = \epsilon_{pp\pi^-}(T_n, \theta_\pi^*, M_{pp}). \quad (15)$$

This function was a main input in the analysis in order to determine the invariant mass and pion angular distributions as well as the integrated cross sections. It was smoothed in order to minimize additional fluctuations in the data due to the limited Monte Carlo statistics. The average efficiency was of the order of 0.3 with a typical uncertainty of about 3%. The reconstruction efficiency  $\epsilon_{pp\pi^-}$  shows a strong dependence as a function of  $M_{pp}$  (see Sec.5.1). It drops towards the two-proton mass, since in this phase space region the two proton tracks are close together. In particular, for pions emitted in the backward direction, the value of  $\epsilon_{pp\pi^-}$  at small proton-proton invariant masses is only of the order of a few percent. The identical detector Monte-Carlo simulation was used to determine the reconstruction efficiency function  $\epsilon(T_n, \theta_n^*)$  for elastic  $np$  scattering.

#### 4.8 Elastic $np$ scattering

For detector calibration purposes and the neutron flux normalisation,  $np$  scattering events from the minimum bias trigger sample were selected. Assuming the elastic  $np$  scattering kinematics for events with one reconstructed track to be valid, the expected time-of-flight  $TOF_n^{\text{exp}}$  for the incoming neutron was calculated using the measured track angle  $\theta_p$  and the velocity  $\beta_1^p$ . Fig.8 shows the difference  $\Delta TOF_n = TOF_n^{\text{exp}} - TOF_n + i \cdot 19.75 \text{ ns}$ ,  $i = 0, 1, \dots$ , between the expected and measured neutron time-of-flight for data with full and empty target cell. Elastic  $np$  scattering events kinematics gave values well-located at  $i \cdot 19.75 \text{ ns}$  and were selected by the indicated cuts. For  $i = 0, 1$ , the neutron time-of-flight corresponds to a neutron kinetic energy above the pion production threshold. The main part of entries between the signal peaks is originating from reactions on the Kapton walls and drift chamber materials. The remaining background part is likely due to inelastic reactions in the liquid hydrogen target like  $np \rightarrow d\pi^0$  or  $np \rightarrow np\pi^0$  and was estimated to be about 1%.

### 5 Results and discussion

Differential cross sections as a function of the proton-proton invariant mass  $M_{pp}$  and the pion c.m. angle  $\theta_\pi^*$  and integrated cross sections were determined from the data. The  $M_{pp}$  and angular distributions were subdivided in

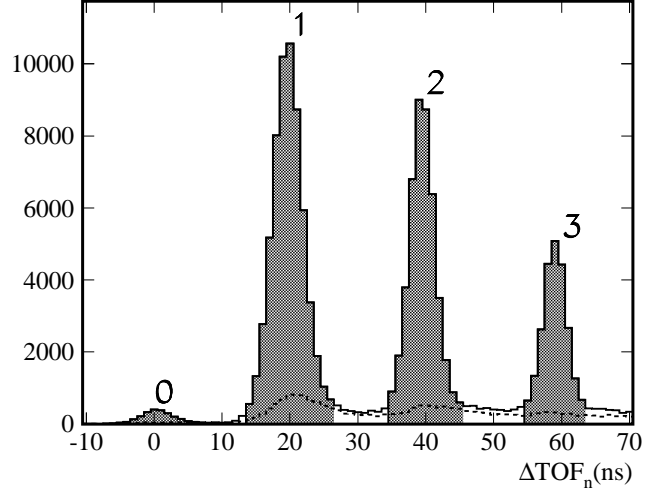


**Fig. 8.**  $\Delta TOF_n$  distribution for data with full and empty (dashed line) target cell. Events within the indicated cuts (in grey) were accepted as elastic  $np$  scattering events.

nine neutron energy bins where the first bin was between threshold and 330 MeV while the other bins were of 30 MeV width. For the determination of the integrated cross sections, a finer binning of 10 MeV width was chosen in order to investigate the energy dependence of the  $\sigma_{np \rightarrow pp\pi^-}$  cross section in more detail. The differential cross sections  $d\sigma/dM_{pp}$  and  $d\sigma/d\theta_\pi^*$  have been normalised to yield the integrated cross section values at the corresponding neutron energies as given in Sec.5.3.

#### 5.1 Invariant mass distributions

The background subtracted and efficiency corrected  $M_{pp}$  distributions for the nine neutron energy bins are shown in Fig. 9. The drawn errors include the statistical error as well as a 3% systematic uncertainty due to the efficiency function  $\epsilon_{pp\pi^-}(T_n, M_{pp})$ . The latter dominates for neutron energies above 345 MeV. For all energies the measured distributions differ significantly from the phase space expectation. At higher energies, this is expected since the excitation of the  $\Delta$  resonance contributes significantly to the production cross section  $\sigma_{11}$  [35]. The strong final state interaction in the  $pp(^1S_0)$  final state affects the Ss ( $\sigma_{11}$ ) and Sp ( $\sigma_{01}$ ) partial waves as already observed in the  $\sigma_{11}$  cross section [1]. Therefore, an enhancement at small  $M_{pp}$  values at least from the Ss partial wave is expected for neutron beam energies near threshold and is in fact observed in the data. For a qualitative understanding, the  $M_{pp}$  distribution from a Ss partial wave at  $T_n = 315 \text{ MeV}$  is included in Fig.9 where the detector resolution and the  $pp(^1S_0)$  final state interaction have been taken into account. The final state interaction was calculated in the effective range approximation [57] where the scattering length  $a_S = -7.8098 \text{ fm}$  and the effective range  $r_{\text{eff}} = 2.767 \text{ fm}$  were taken from Ref. [58]. Distributions

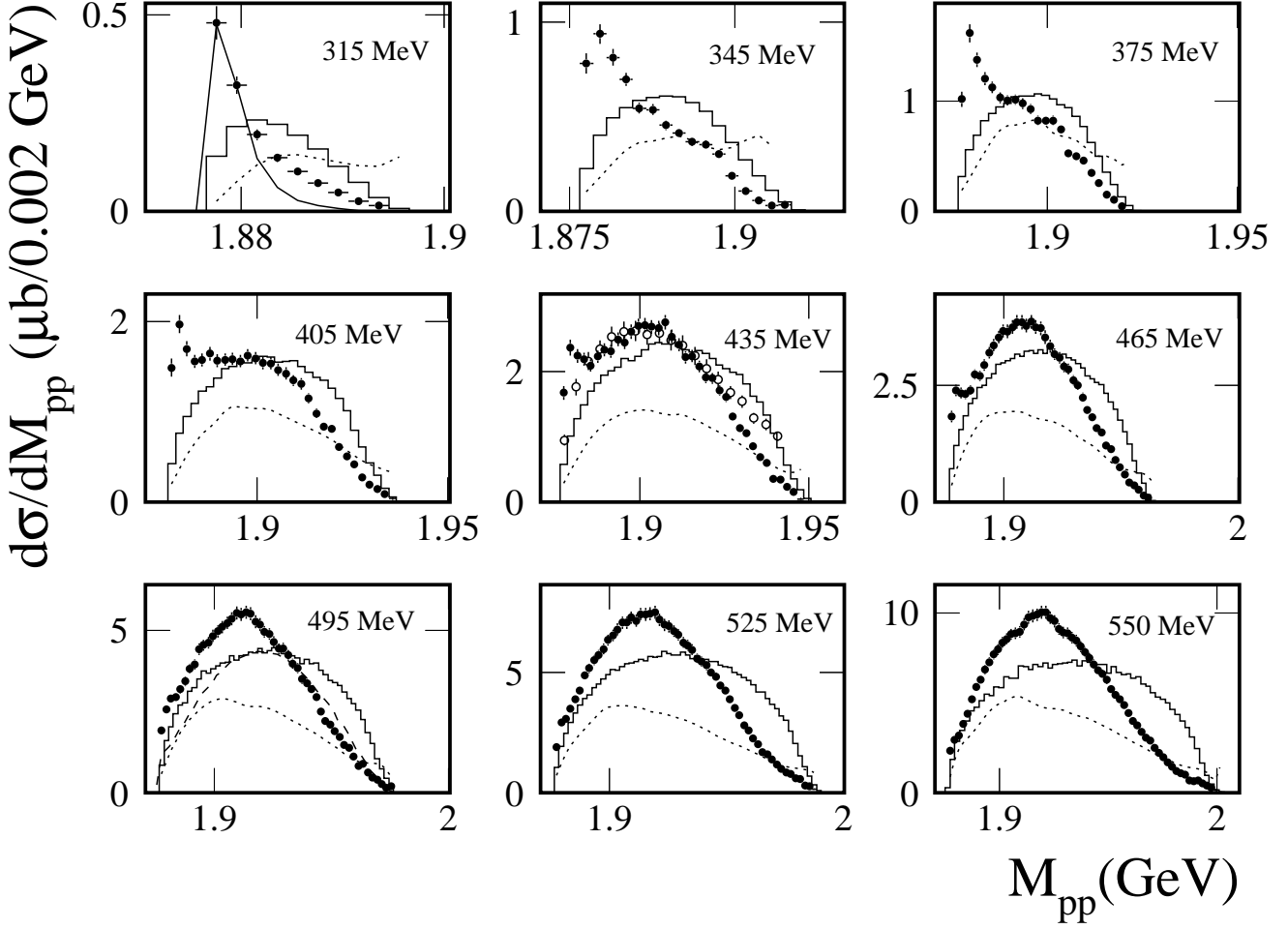


**Fig. 9.** Full dots: differential cross sections  $d\sigma/dM_{pp}$  after background subtraction and efficiency correction. Histograms: normalised phase space expectations. Dotted lines: smoothed efficiency functions  $\epsilon_{pp\pi^-}(T_n, M_{pp})$  after integration over  $\cos\theta_\pi^*$  where  $\epsilon_{pp\pi^-}(T_n, M_{pp}) = 1$  corresponds to the maximum value of the ordinate. At 315 MeV, the  $M_{pp}$  distribution from a Ss partial wave, scaled to the maximum of the measured data, is shown as a solid line. Data for the reaction  $np \rightarrow pp\pi^-$  at 443 MeV [40] are shown as open circles. Dashed line:  $d\sigma/dM_{pp}$  for the reaction  $pp \rightarrow pp\pi^0$  at 500 MeV [61].

produced by Sp partial waves from  $\sigma_{01}$  or Sd partial waves from  $\sigma_{11}$  would give a similar and even narrower signal.

The  $\sigma_{01}$  contribution to the  $M_{pp}$  distribution at  $T_n = 315$  MeV has been estimated by a comparison to the reaction  $pp \rightarrow pp\pi^0$ . The  $M_{pp}$  distribution at 315 MeV, scaled by a factor of 2 due to (2), is shown in Fig. 10 together with a measurement of the reaction  $pp \rightarrow pp\pi^0$  at  $T_p = 310$  MeV [60] which can be described by a combination of Ss, Ps, Pp and Sd contributions [60]. Both distributions differ in shape and magnitude which clearly indicates the presence of  $\sigma_{01}$  in the reaction  $np \rightarrow pp\pi^-$ . The difference of 5 MeV in beam energies is slightly less than required for a comparison in the Q- or  $\eta$ -scheme ( $\approx 7$  MeV). This has been partly compensated by scaling the  $M_{pp}$  distribution at 315 MeV to the cross section value

at 317 MeV by interpolating the cross section results for 315 MeV and 325 MeV from Sec. 5.3. The neutron energy bin width of about 40 MeV leads to entries for the reaction  $np \rightarrow pp\pi^-$  beyond the kinematical limit for  $M_{pp}$  from the reaction  $pp \rightarrow pp\pi^0$ . Both distributions were subtracted in order to extract the  $\sigma_{01}$  contribution. Negative values are likely due to the mismatch of the beam energies. By integrating the positive values, a  $\sigma_{01}$  cross section of about  $0.9 \mu\text{b}$  was found to be compared to a  $\sigma_{11}$  value of about  $4.3 \mu\text{b}$  at  $T_p = 310$  MeV [60]. For a comparison, the  $M_{pp}$  distribution from a Sp partial wave is shown. Again the detector resolution and the  $^1S_0$  final state interaction, calculated in the effective range approximation, have been taken into account. The normalisation was chosen in order to yield the same  $\sigma_{01}$  cross section

value of  $0.9 \mu\text{b}$ . The good agreement between the  $\sigma_{01}$  and the Sp distribution indicates that close to threshold the cross section  $\sigma_{01}$  is mainly driven by Sp partial waves.

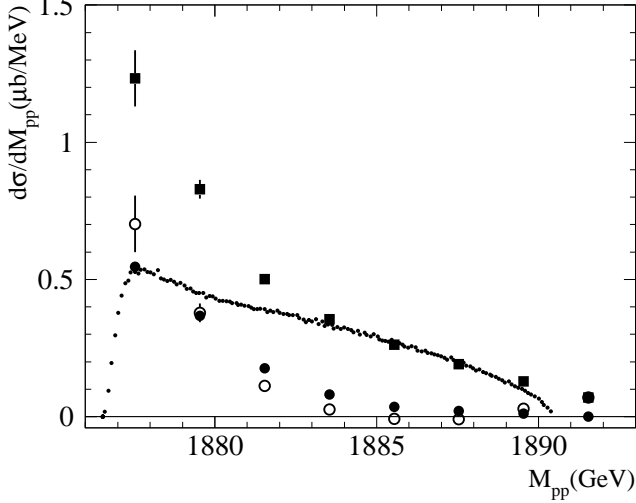


**Fig. 10.** Full boxes:  $d\sigma/dM_{pp}$  at 315 MeV rescaled to give the integrated cross section at 317 MeV (see text) and multiplied by a factor of two. Small dots:  $d\sigma/dM_{pp}$  for the reaction  $pp \rightarrow pp\pi^0$  at 310 MeV [60]. Open circles: difference between both distributions. Full dots:  $M_{pp}$  distribution produced by a Sp partial wave taking into account detector resolution and final state interaction calculated in the effective range approximation.

Data of the experiment of Bachman et al. [40] for the reaction  $np \rightarrow pp\pi^-$  measured at 443 MeV are included in Fig. 9. Since the authors have published only relative cross sections, we normalised their distribution to our data. Their data also do not fit the phase space expectation but in addition show a strong deviation from our  $M_{pp}$  distribution at higher  $M_{pp}$  values and as well near the two-proton mass. Due to the clear signal observed by Handler [28] at 409 MeV, a  $^1S_0$  enhancement at small  $M_{pp}$  values has been expected [59]. The missing  $^1S_0$  enhancement in the Bachman data was attributed to the poor invariant mass resolution which might dilute the signal [59]. However, it might be also due to an overestimation of the efficiency function in this particular phase space region. It should be noted that the result of Handler, given as a function of  $r = p_\pi^*/p_{\pi,\text{max}}^*$ , is in good agreement with the shape of our data [45].

At 495 MeV, the  $M_{pp}$  distribution is compared to the  $M_{pp}$  distribution of the reaction  $pp \rightarrow pp\pi^0$  at  $T_p = 500 \text{ MeV}$  [61] rescaled by a factor of 1/2 (see Sect.2). Since the  $M_{pp}$  distributions for both reactions differ significantly, one can conclude that  $\sigma_{01}$  gives also a large contribution to the reaction  $np \rightarrow pp\pi^-$  at higher energies where the  $\sigma_{11}$  cross section is already influenced by the excitation of the  $\Delta$  resonance.

## 5.2 Angular distributions

The differential cross sections  $d\sigma_{np \rightarrow pp\pi^-}/d\Omega^*$  for the nine neutron energies are shown in Fig. 11 and Tab.3. Corrections for reconstruction efficiency have been applied and background has been subtracted. For all energies, the angular distributions are anisotropic and at lower energies, a pronounced f/b-asymmetry is observed. The solid curves are the results of a fit according to (11). The resulting anisotropy parameters  $b_{np \rightarrow pp\pi^-}$ , displayed in Fig. 12, show a strong dependence in  $T_n$  with a maximum of 0.6 at 375 MeV and a shallow minimum of 0.37 at 495 MeV. Compared to former experiments, the results show a substantial improvement. Below 570 MeV, only two other experiments, at 409 MeV [28] and 435 MeV [40], have measured over the full angular range. Our  $b_{np \rightarrow pp\pi^-}$  values are in quantitative contradiction to the data of Handler [28], Kleinschmidt et al. [31] and Bannwarth et al. [39].

The inclusive experiments of Kleinschmidt et al. [31] as well as Bannwarth et al. [39] did a pioneering work in establishing the existence of  $\sigma_{01}$  but have some shortcomings. Both experiments were restricted in acceptance and their analyses relied on a model dependent extrapolation of the pion momentum spectra to small values. In the experiment of Kleinschmidt et al. [31], positive charged pions were measured in the forward direction up to  $\theta_\pi^* \approx 30^\circ$  only, which makes a reliable extraction of the angular distribution parameters difficult. In fact, the fits to the angular distributions were performed by setting the f/b-asymmetry parameter  $a$  identically zero. In the experiment of Bannwarth et al. [39], positive and negative pions were measured at  $\theta_\pi^* = 90^\circ$  and  $\theta_\pi^* = 166^\circ$ . From these cross section values, the angular distribution parameters  $a_1$  and  $b_{np \rightarrow pp\pi^-}$  were determined using (9). However, no explicit  $\pi^\pm$  identification was performed and hence, systematic errors might have been underestimated.

The measured anisotropy parameters  $b_{np \rightarrow pp\pi^-}$  are significantly larger than those found in the reaction  $pp \rightarrow pp\pi^0$ , as shown in Fig. 13. This is in qualitative agreement with most of the former findings, as can be seen from the comparison of the results of older np experiments, shown in Fig. 12, with the  $b_{pp \rightarrow pp\pi^0}$  values in Fig.13. This still holds when our data are compared only to the more recent  $b_{pp \rightarrow pp\pi^0}$  values of Rappenecker et al. [32] which are larger than the values of Dunaitsev et al. [62] and Stanislaus et al. [61].

The asymmetry parameters  $a$  shown in Fig. 14 decreases monotonically with increasing energy which was already indicated by former experiments. However, quantitatively, the Bannwarth results [39] again deviate significantly from our data. Bachman et al. [40] reported no significant f/b-asymmetry at 435 MeV but did not give a numerical value. We have fitted the angular distribution of Bachman et al. [40] according to (11). We reproduced their value  $b_{np \rightarrow pp\pi^-} = 0.47 \pm 0.06$  (Fig. 12) and found  $a = 0.055 \pm 0.024$  (Fig. 14).

The small value for  $a$  in the data of Bachman et al. [40] might be attributed to the missing signal of the  $pp(^1S_0)$

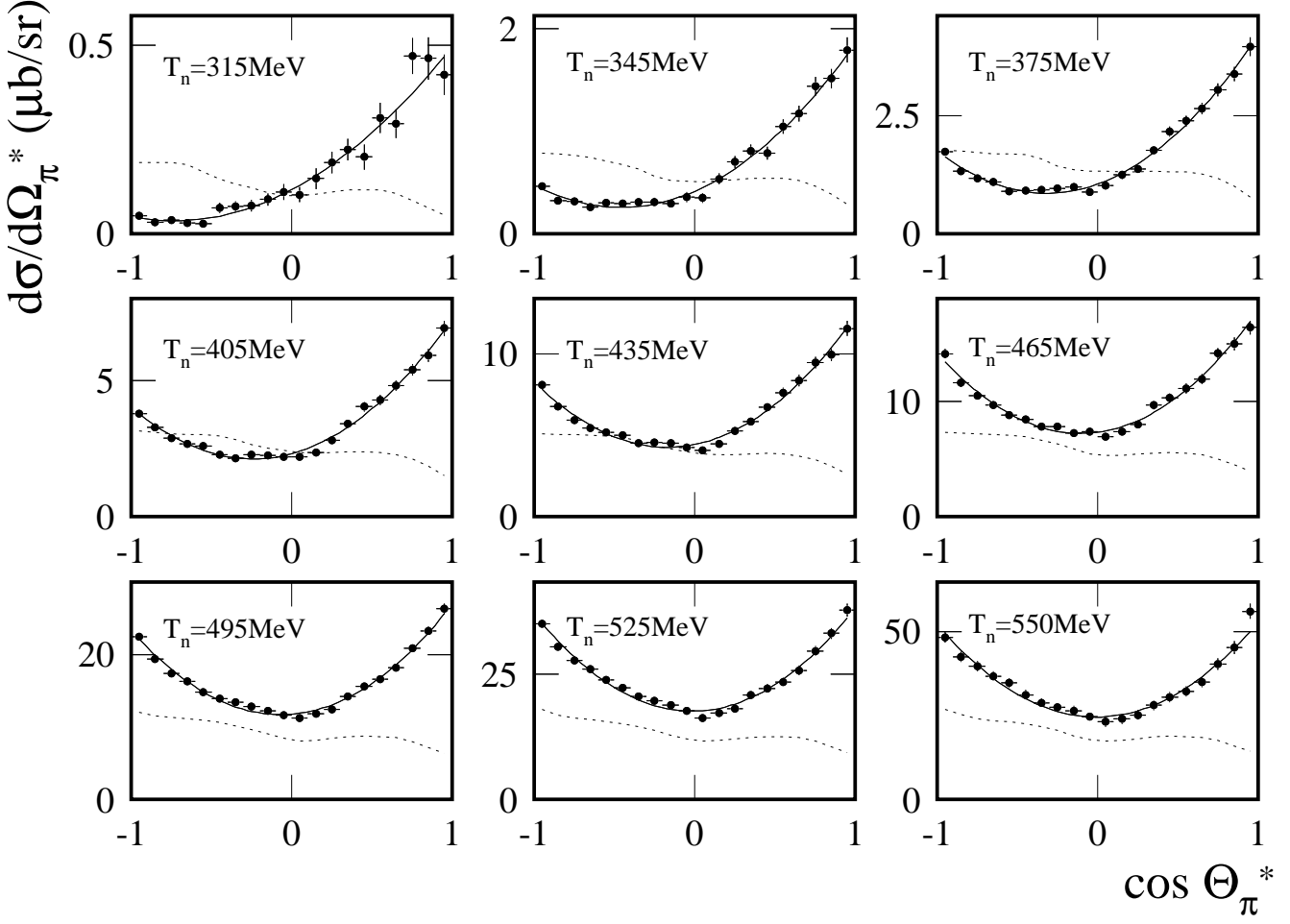


**Fig. 11.** Full dots: Differential cross sections  $d\sigma/d\Omega_\pi^*$  after background subtraction and efficiency correction. Dotted lines: smoothed efficiency functions  $\epsilon_{pp\pi^-}(T_n, \cos\theta_\pi^*)$  after integration over  $M_{pp}$  where  $\epsilon_{pp\pi^-}(T_n, \cos\theta_\pi^*) = 1$  corresponds to the maximum value of the ordinate. Full lines: results of a fit according to (11).

final state interaction in their  $M_{pp}$  spectrum. If their efficiency function underestimated the contribution of this particular phase space region, the effect of the (I=0)-(I=1) interference between Ss and Sp partial waves would be suppressed.

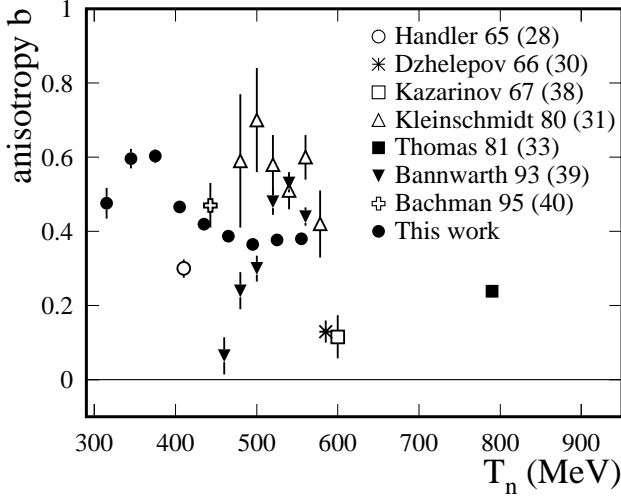
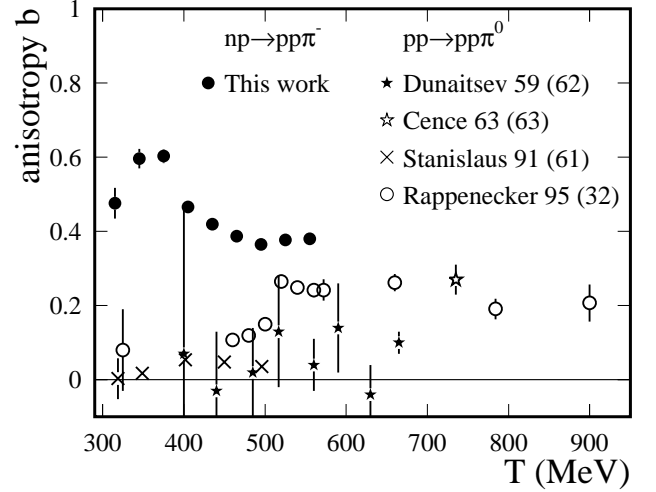
Both parameters,  $a$  and  $b_{np \rightarrow pp\pi^-}$ , clearly indicate the significant contribution of the isoscalar production cross section  $\sigma_{01}$  in the reaction  $np \rightarrow pp\pi^-$ , in particular in the energy range between 315 MeV and 400 MeV.

The excitation of Pp(I=0) partial waves are expected to be suppressed at small energies due to their  $\eta^8$  dependence and the anisotropies  $b_{pp \rightarrow pp\pi^0}$  were measured to be small for energies below 450 MeV. Since the partial wave  $^3S_1 \rightarrow ^1S_0 p_1$  leads to a flat distribution in  $\cos\theta_\pi^*$ , only the partial wave  $^3D_1 \rightarrow ^1S_0 p_1$  could explain the large  $b_{np \rightarrow pp\pi^-}$  values for energies below 450 MeV. The decreasing  $b_{np \rightarrow pp\pi^-}$  values above about 375 MeV might be un-

derstood in terms of increasing contributions from Ps partial waves in the I=1 channel. The relative cross section from Ps partial waves in the reaction  $np \rightarrow pp\pi^-$  was found to increase from 18% to 30% between  $T_p = 325$  MeV and  $T_p = 400$  MeV [64]. The  $b$  parameter tends to be constant above 450 MeV which can be understood in terms of increasing Pp partial waves from the isospin amplitude  $M_{11}$  being reflected in the rising of  $b_{pp \rightarrow pp\pi^0}$  observed by Rappenecker et al. [32].

The large f/b-asymmetries are likely due to the interference between the Sp partial waves from the isospin amplitude  $M_{10}$  and Ss from  $M_{11}$ . This is in agreement with the TRIUMF experiments [43,44] which have measured the Ss and Sp contributions in the reaction  $pn \rightarrow pp\pi^-$  at very small  $M_{pp}$  values. With increasing energy, the interference signal vanishes rapidly. This can be understood by the relative increase of the Ps and Pp partial waves in the I=1

$\cos \theta_\pi^*$	315 MeV	345 MeV	375 MeV	405 MeV	435 MeV	465 MeV	495 MeV	525 MeV	550 MeV
-0.95	$0.046 \pm 0.010$	$0.460 \pm 0.043$	$1.73 \pm 0.10$	$3.77 \pm 0.19$	$8.12 \pm 0.38$	$14.2 \pm 0.6$	$22.5 \pm 0.9$	$35.0 \pm 1.5$	$48.3 \pm 2.3$
-0.85	$0.031 \pm 0.010$	$0.319 \pm 0.036$	$1.32 \pm 0.09$	$3.28 \pm 0.17$	$6.80 \pm 0.35$	$11.7 \pm 0.6$	$19.4 \pm 0.8$	$30.5 \pm 1.3$	$42.4 \pm 2.1$
-0.75	$0.036 \pm 0.010$	$0.316 \pm 0.034$	$1.17 \pm 0.08$	$2.88 \pm 0.16$	$5.92 \pm 0.31$	$10.5 \pm 0.5$	$17.5 \pm 0.8$	$27.8 \pm 1.3$	$39.7 \pm 2.0$
-0.65	$0.027 \pm 0.009$	$0.259 \pm 0.032$	$1.09 \pm 0.08$	$2.66 \pm 0.15$	$5.43 \pm 0.30$	$9.69 \pm 0.48$	$16.3 \pm 0.7$	$26.1 \pm 1.2$	$36.7 \pm 1.9$
-0.55	$0.026 \pm 0.011$	$0.298 \pm 0.037$	$0.90 \pm 0.07$	$2.59 \pm 0.15$	$5.17 \pm 0.29$	$8.85 \pm 0.45$	$14.8 \pm 0.7$	$23.9 \pm 1.1$	$34.7 \pm 1.8$
-0.45	$0.067 \pm 0.013$	$0.291 \pm 0.036$	$0.91 \pm 0.07$	$2.29 \pm 0.14$	$5.00 \pm 0.28$	$8.46 \pm 0.44$	$14.0 \pm 0.6$	$22.4 \pm 1.1$	$31.2 \pm 1.8$
-0.35	$0.072 \pm 0.014$	$0.306 \pm 0.037$	$0.93 \pm 0.07$	$2.14 \pm 0.13$	$4.50 \pm 0.26$	$7.83 \pm 0.43$	$13.4 \pm 0.6$	$20.6 \pm 1.0$	$28.7 \pm 1.7$
-0.25	$0.074 \pm 0.015$	$0.303 \pm 0.043$	$0.95 \pm 0.08$	$2.27 \pm 0.14$	$4.58 \pm 0.28$	$7.80 \pm 0.43$	$12.9 \pm 0.6$	$19.7 \pm 1.0$	$27.5 \pm 1.6$
-0.15	$0.090 \pm 0.017$	$0.291 \pm 0.041$	$0.98 \pm 0.08$	$2.26 \pm 0.15$	$4.51 \pm 0.28$	$7.28 \pm 0.41$	$12.3 \pm 0.6$	$18.9 \pm 1.0$	$26.5 \pm 1.7$
-0.05	$0.110 \pm 0.021$	$0.355 \pm 0.047$	$0.88 \pm 0.08$	$2.18 \pm 0.15$	$4.27 \pm 0.28$	$7.37 \pm 0.43$	$11.7 \pm 0.6$	$17.7 \pm 1.0$	$24.7 \pm 1.6$
0.05	$0.103 \pm 0.020$	$0.345 \pm 0.047$	$1.01 \pm 0.08$	$2.19 \pm 0.16$	$4.10 \pm 0.28$	$6.94 \pm 0.43$	$11.3 \pm 0.6$	$16.3 \pm 1.0$	$23.1 \pm 1.6$
0.15	$0.146 \pm 0.028$	$0.533 \pm 0.055$	$1.25 \pm 0.10$	$2.35 \pm 0.16$	$4.49 \pm 0.29$	$7.38 \pm 0.45$	$11.9 \pm 0.6$	$17.3 \pm 1.0$	$24.0 \pm 1.6$
0.25	$0.189 \pm 0.030$	$0.695 \pm 0.064$	$1.36 \pm 0.10$	$2.80 \pm 0.17$	$5.29 \pm 0.32$	$8.01 \pm 0.45$	$12.5 \pm 0.6$	$18.1 \pm 1.0$	$25.2 \pm 1.6$
0.35	$0.223 \pm 0.030$	$0.803 \pm 0.067$	$1.76 \pm 0.11$	$3.42 \pm 0.19$	$5.87 \pm 0.33$	$9.73 \pm 0.51$	$14.2 \pm 0.7$	$20.9 \pm 1.1$	$28.1 \pm 1.7$
0.45	$0.203 \pm 0.034$	$0.781 \pm 0.069$	$2.16 \pm 0.13$	$4.03 \pm 0.22$	$6.73 \pm 0.36$	$10.3 \pm 0.5$	$15.7 \pm 0.7$	$22.1 \pm 1.2$	$30.5 \pm 1.8$
0.55	$0.308 \pm 0.042$	$1.04 \pm 0.08$	$2.38 \pm 0.14$	$4.27 \pm 0.23$	$7.64 \pm 0.40$	$11.2 \pm 0.6$	$16.6 \pm 0.8$	$23.4 \pm 1.2$	$32.2 \pm 1.9$
0.65	$0.292 \pm 0.040$	$1.17 \pm 0.09$	$2.65 \pm 0.15$	$4.81 \pm 0.25$	$8.37 \pm 0.45$	$11.9 \pm 0.6$	$18.2 \pm 0.8$	$25.8 \pm 1.3$	$35.0 \pm 2.0$
0.75	$0.472 \pm 0.051$	$1.44 \pm 0.11$	$3.04 \pm 0.17$	$5.39 \pm 0.28$	$9.49 \pm 0.49$	$14.2 \pm 0.7$	$21.0 \pm 0.9$	$29.7 \pm 1.4$	$40.3 \pm 2.2$
0.85	$0.465 \pm 0.058$	$1.51 \pm 0.11$	$3.38 \pm 0.19$	$5.92 \pm 0.31$	$9.96 \pm 0.52$	$15.0 \pm 0.8$	$23.3 \pm 1.0$	$33.2 \pm 1.6$	$45.2 \pm 2.5$
0.95	$0.422 \pm 0.055$	$1.79 \pm 0.14$	$3.96 \pm 0.24$	$6.92 \pm 0.37$	$11.6 \pm 0.6$	$16.4 \pm 0.8$	$26.4 \pm 1.2$	$37.9 \pm 1.8$	$56.0 \pm 3.0$

**Table 3.** Differential cross sections  $d\sigma/d\Omega_\pi^*$  in  $\mu\text{b}/\text{sr}$ .**Fig. 12.** Anisotropy parameter  $b_{np \rightarrow pp\pi^-}$  compared to other  $np \rightarrow NN\pi^\pm$  experiments [28, 30, 38, 31, 33, 39, 40].**Fig. 13.** Anisotropy parameters  $b_{np \rightarrow pp\pi^-}$  compared to  $pp \rightarrow pp\pi^0$  experiments [62, 63, 61, 32].

channel. In addition, due to the expected  $\eta$ -dependence, the partial waves ratio Ss/Sp is supposed to drop with increasing beam energy.

### 5.3 Integrated cross sections

The  $N_{np \rightarrow pp\pi^-}$  yields were obtained for each neutron energy bin  $T_n$  by integrating the events over  $M_{pp}$  and  $\cos \theta_\pi^*$  weighting each event by  $\epsilon_{pp\pi^-}^{-1}(T_n, M_{pp}, \cos \theta_\pi^*)$ , the inverse of the appropriate efficiency function value. The cross sections were calculated from

$$\sigma_{np \rightarrow pp\pi^-} = \frac{N_{np \rightarrow pp\pi^-}}{L} \frac{1}{f}, \quad (16)$$

where  $f$  is the lifetime factor of the data acquisition system. The time-integrated luminosity  $L$  is given by the product  $L = N_n \cdot F_p$ , where  $F_p$  denotes the number of protons per unit area and  $N_n$  the time-integrated number of neutrons incident on the liquid hydrogen target. It was obtained by measuring the number of elastic  $np$  scattering events in the minimum bias trigger sample at a given neutron energy and neutron c.m. angle  $\theta_n^*$ :

$$L(T_n, \theta_n^*) = \frac{N_{np \rightarrow np}}{\Delta\Omega^* \cdot \frac{d\sigma_{np \rightarrow np}}{d\Omega^*}} \frac{1}{f \cdot P \cdot \epsilon(T_n, \theta_n^*)}. \quad (17)$$

The efficiency function  $\epsilon(T_n, \theta_n^*)$  for elastic  $np$  scattering was determined from the Monte Carlo simulation in steps of 10 MeV for  $T_n$  and  $10^\circ$  for  $\theta_n^*$ , and  $P$  is the prescal-

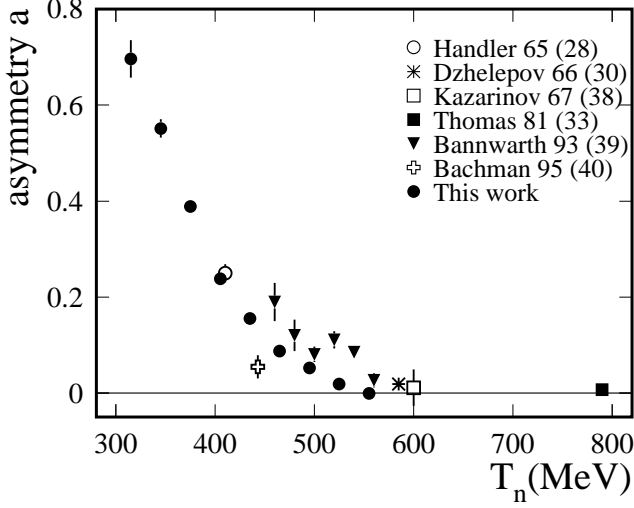


**Fig. 14.**  $f/b$ -asymmetries compared to other  $np \rightarrow pp\pi^-$  experiments [28, 30, 38, 39, 40]. For the value quoted for the experiment of Bachman et al. [40]: see text.

ing factor for the minimum bias trigger. The differential cross sections  $\frac{d\sigma_{np \rightarrow np}}{d\Omega}$  were obtained using the partial wave analysis program SAID of Arndt et al. [65]. Finally, for each neutron energy bin, the luminosity was averaged between  $\theta_n^* = 115^\circ$  and  $155^\circ$ , the acceptance range where the efficiency function was approximately constant. Background contributions from the target surroundings for both, the  $N_{np \rightarrow pp\pi^-}$  (Sec. 4.6) and the  $N_{np \rightarrow np}$  (Sec. 4.8) yields, were subtracted using data taken with an empty target cell. In addition, the  $N_{np \rightarrow np}$  yields were corrected for the estimated background of about 1% due to reactions in the  $LH_2$  target (Sec. 4.8).

Compared to systematic errors statistical errors for the  $\sigma_{np \rightarrow pp\pi^-}$  cross sections were negligible for energies above 325 MeV. A total systematic error of the order of 5.5% was estimated from three sources and these errors were added in quadrature:

1. the error of the efficiency function  $\epsilon_{pp\pi^-}(T_n, M_{pp}, \cos\theta_\pi^*)$  (3 – 4%),
2. uncertainties in the experimental elastic np scattering yields and the efficiency function  $\epsilon(T_n, \theta_n^*)$  (3.5%),
3. the uncertainty of the elastic np scattering differential cross section values (2.5%).

The latter was estimated from the elastic cross section errors provided by the interactive partial wave analysis program SAID [65] (1%) and the difference of the cross section values between the Arndt analysis on one hand and the values given by the Nijmegen group [66] and Bystricky et al. [67] on the other hand. The Nijmegen analysis provides only values below 350 MeV beam energy. The maximum observed deviations between the Nijmegen and the Arndt analysis are of

$T_n$ (MeV)	$\eta$	$Q$ (MeV)	$\sigma_{np \rightarrow pp\pi^-}$	$\Delta\sigma$
295	0.225	3.76	0.000395	0.000196
305	0.339	8.40	0.00143	0.00032
315	0.425	13.03	0.00281	0.00046
325	0.498	17.65	0.00611	0.00073
335	0.563	22.25	0.00923	0.00094
345	0.623	26.85	0.0135	0.0012
355	0.678	31.44	0.0188	0.0016
365	0.730	36.02	0.0236	0.0019
375	0.780	40.58	0.0343	0.0026
385	0.828	45.14	0.0420	0.0031
395	0.873	49.69	0.0542	0.0040
405	0.918	54.22	0.0696	0.0050
415	0.961	58.75	0.0869	0.0061
425	1.003	63.27	0.097	0.007
435	1.043	67.78	0.130	0.009
445	1.083	72.27	0.153	0.010
455	1.122	76.76	0.183	0.012
465	1.161	81.24	0.209	0.014
475	1.198	85.71	0.243	0.016
485	1.235	90.17	0.294	0.019
495	1.272	94.62	0.334	0.021
505	1.308	99.06	0.390	0.025
515	1.343	103.49	0.429	0.027
525	1.378	107.91	0.501	0.032
535	1.413	112.32	0.573	0.036
545	1.447	116.73	0.642	0.040
555	1.480	121.12	0.757	0.047
565	1.514	125.51	0.916	0.057

**Table 4.** Integrated cross sections  $\sigma_{np \rightarrow pp\pi^-}$  in mb.

the order 1%. The differential cross section values at  $\theta_n^* = 135^\circ$  given by the analysis of Bystricky et al. are significantly smaller than those given by the Arndt analysis. The deviation increases in magnitude from 0 at 300 MeV up to -5% at 400 MeV and then decreases down to -1.5% at 560 MeV.

It should be noted that neutron-proton elastic scattering cross section data taken at PSI [68] have been found to be significantly below the values provided by the Arndt analysis as well as the Bystricky analysis. The typical deviation is of the order -5% - -10%.

The integrated cross section  $\sigma_{np \rightarrow pp\pi^-}$  (Fig. 15, Tab. 4) rises in the measured energy range by four orders of magnitude. The new data improve the knowledge of  $\sigma_{np \rightarrow pp\pi^-}$  for energies below 570 MeV substantially.

The cross section measurements for the reaction  $np \rightarrow \pi^+ X$  by Kleinschmidt et al. [31] which dominated the data between 480 MeV and 580 MeV so far are systematically below our data. This might be related to the above mentioned acceptance cuts in their experiment. In addition, due to the different particle masses in the final states of the reactions  $np \rightarrow pp\pi^-$  and  $np \rightarrow nn\pi^+$ , the cross section data can not be compared at the same beam energies. The  $T_n$  values of Kleinschmidt et al. have to be lowered by about 6 MeV if the comparison would be performed in the  $\eta$ -scheme resulting in a reduction of the observed



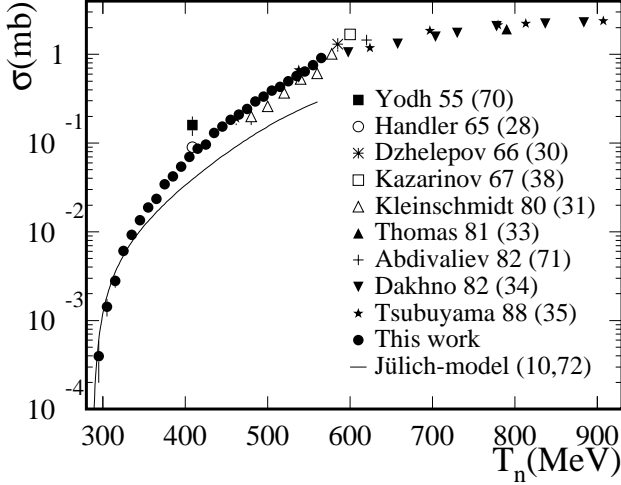


**Fig. 15.** Measured integrated cross section  $\sigma_{np \rightarrow pp\pi^-}$  as a function of beam energy compared to other  $np \rightarrow NN\pi^\pm$  experiments [70, 28, 30, 38, 31, 33, 71, 34, 35]. Full line: prediction of the Jülich model [10, 72].

deviation. Moreover, their data have to be corrected if improved cross section measurements are taken into account. For the normalisation of their yields, the authors used cross section values of the reaction  $np \rightarrow d\pi^0$ . Those were determined by Hürster et al. [69] using the relation  $\sigma_{np \rightarrow d\pi^0} = \frac{1}{2}\sigma_{pp \rightarrow d\pi^+}$ . Since this relation is only exact under the assumption of isospin invariance, several corrections due to the different particle masses and the Coulomb interaction in the  $pp^-$  and  $d\pi^+$  system have to be applied. In consideration of the actual precise  $pp \rightarrow d\pi^+$  data and all relevant corrections, the  $\sigma_{np \rightarrow d\pi^0}$  values of Hürster et al. [69] are too low by about 10% at 580 MeV and 20% at 480 MeV [68]. This results in an equivalent underestimation of the  $\sigma_{np \rightarrow \pi^+ X}$  cross sections. If all these effects are taken into account, our cross sections and the Kleinschmidt data are found to be compatible. Nevertheless, the differences between our anisotropy parameters and those found by Kleinschmidt et al. still remain since the determination of the anisotropy parameter does not depend on the flux normalisation.

The most precise measurement at low energies, the data point of Handler [28] at 409 MeV, is significantly above our cross section values. This measurement averaged over a broad neutron energy spectrum where the mean neutron energy was determined by a maximum likelihood fit. It should be noted that the fit result for the neutron energy spectrum lies slightly below the measured neutron energy spectrum [28]. As a consequence, the average neutron energy quoted by Handler might be underestimated.

Our  $\sigma_{np \rightarrow pp\pi^-}$  cross sections were also compared to the predictions of the Jülich model [10, 72] given as a full line in Fig. 15. At small neutron energies, the model overestimates slightly the data points. Above  $T_n \approx 320$  MeV ( $\eta \approx 0.5$ ), the model underestimates our cross sections

$i$	$c_i$	$\Delta c_i$
0	0.0079057	0.000059489
1	-0.10483	0.00037957
2	0.50387	0.0012598
3	-0.92768	0.0031263
4	0.65065	0.0027194

**Table 5.** Fit parameters for  $\sigma_{11}$ .

more and more as the energy increases with a maximum deviation of a factor 2.5 at the largest energies.

#### 5.4 Extraction of $\sigma_{01}$

From the measured  $\sigma_{np \rightarrow pp\pi^-}$  cross sections,  $\sigma_{01}$  was calculated using (2). The cross section  $\sigma_{11}$  as a function of  $\eta$  was determined by a fourth order polynomial fit

$$\sigma_{11}(\eta) = \sum_{i=0}^4 c_i \eta^i \quad (18)$$

to the cross section data  $\sigma_{pp \rightarrow pp\pi^0}$  of Meyer et al. [1], Bondar et al. [24], Rappenecker et al. [32], Stanislaus et al. [61] and Dunaitsev et al. [62] between  $T_p = 285$  MeV and  $T_p = 572$  MeV. The results of the fit parameters were mainly determined by the data sets of Meyer et al. [1] and Bondar et al. [24] for  $\eta < 0.6$ , and Rappenecker et al. [32] for  $\eta > 1.15$ . The data of Dunaitsev et al. [62] and Stanislaus et al. [61] which are filling the intermediate  $\eta$  range were needed for the proper convergence of the fit. The reduced  $\chi^2$  value of  $\chi_\nu^2 = 2.165$  with  $\nu = 63$  degrees of freedom indicates some inconsistencies in the  $\sigma_{pp \rightarrow pp\pi^0}$  data sets. The resulting fit parameters are listed in Tab. 5 and the result is shown in Fig. 16.

The subtraction procedure according to (2) was performed within the  $\eta$ - and the  $Q$ -scheme. The extracted  $\sigma_{01}$ -values are shown in Fig. 16 as a function of  $\eta$ . The errors were calculated from the propagated  $\sigma_{np \rightarrow pp\pi^-}$  uncertainties. The different results for  $\sigma_{01}$  found by the two methods are a measure of the systematic uncertainty induced by the different model assumptions.

The obtained  $\sigma_{01}$ -values are reasonably described by a function of the form  $\sigma_{01} \propto \eta^4$ , as demonstrated by the solid line in Fig. 16, except for the near-threshold region. The  $\eta^4$  dependence strongly supports that  $\sigma_{01}$  is only carried by partial waves of the  $S_p$  type in the energy range below 570 MeV and confirms the interpretation of the  $M_{pp}$  spectrum at 315 MeV. This finding is in contrast to the  $\eta^{9.1 \pm 2.4}$  dependence found by Kleinschmidt et al. [31]. Due to the large exponent, the authors concluded that mainly  $P_p$  partial waves should contribute to the isoscalar cross section. However, this strong  $\eta$  dependence was caused by the above mentioned incorrect normalisation of the cross sections.

The observed deviation of  $\sigma_{01}$  from the  $\eta^4$  behaviour near threshold might be addressed to the  $pp(^1S_0)$  final state interaction. The modification of the cross section  $\sigma_{11}$  near

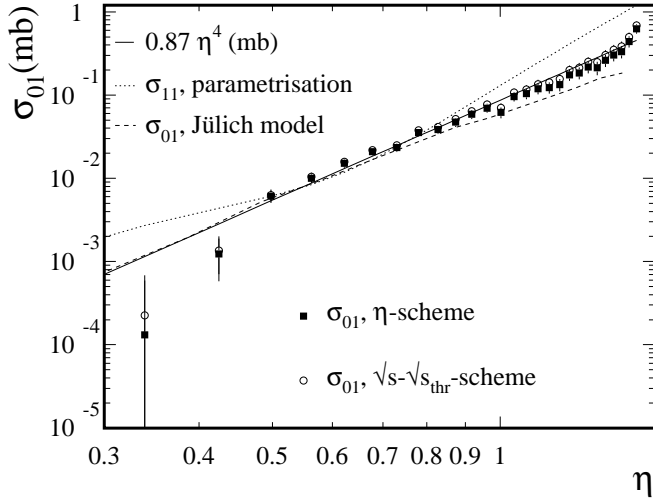


**Fig. 16.** The extracted cross section  $\sigma_{01}$  in the  $\eta$ - (full boxes) and  $Q$ -scheme (open circles) as a function of  $\eta$ . Drawn as a full line is a function proportional to  $\eta^4$ . For comparison, the parametrized  $\sigma_{11}$  cross section (see text) is shown as a dotted line. The dashed line is  $\sigma_{01}$  as predicted by the Jülich model (see text).

threshold due to the  $pp(^1S_0)$  final state interaction is already known [1]. However, the modification of the cross section  $\sigma_{11}$  was mainly observed at much smaller values of  $\eta$  [1].

In the range  $0.5 < \eta < 0.9$ , the  $\sigma_{01}$  cross section is at least of the same order as  $\sigma_{11}$  or even larger. This is the same region where the anisotropy parameters  $b_{np \rightarrow pp\pi^-}$  and the  $f/b$ -asymmetries are very large which supports their interpretation given in Sec. 5.2. In this context, it is interesting to note that meson production models predict a dynamical suppression of the  $Ss$  partial wave [5, 72] in the same energy region. At higher values of  $\eta$ , the resonant production with a  $\Delta N$  intermediate state contributes more and more [35] and hence,  $\sigma_{11}$  increases much stronger than  $\sigma_{01}$ . Nevertheless,  $\sigma_{01}$  is found to contribute still about 30% to the total  $\sigma_{np \rightarrow pp\pi^-}$  cross section.

Using the cross sections  $\sigma_{np \rightarrow pp\pi^-}$  and  $\sigma_{pp \rightarrow pp\pi^0}$  predicted by the Jülich model [10, 72], the cross section  $\sigma_{01}$  was calculated in the  $\eta$ -scheme. As compared to  $\sigma_{np \rightarrow pp\pi^-}$  (see Fig. 15), the cross section  $\sigma_{01}$  is much better reproduced by the Jülich model (dashed line in Fig. 16), although the excitation function shows a flatter slope than a  $\eta^4$  function resulting in a 50% underestimation of the cross section  $\sigma_{01}$  at the largest energies. The underestimation of the  $\sigma_{np \rightarrow pp\pi^-}$  cross section at higher energies is mainly caused by the problem to describe the  $\sigma_{11}$  cross section, in particular the higher partial waves  $P_s$  and  $P_p$  [64].

## 6 Conclusion

We have measured the reaction  $np \rightarrow pp\pi^-$  for neutron energies from threshold up to 570 MeV. Differential and

integrated cross sections over four orders of magnitude have been determined resulting in a substantial improvement of the data compared to former measurements. A consistent picture of the reaction  $np \rightarrow pp\pi^-$  has been found where all results establish the significant contribution of the isoscalar cross section  $\sigma_{01}$  to the reaction  $np \rightarrow pp\pi^-$  over the whole energy range. The determination of the cross section  $\sigma_{01}$  using the data of the reaction  $pp \rightarrow pp\pi^0$  shows that  $\sigma_{01}$  is mainly carried by  $S_p$  partial waves. The Jülich model is able to describe the near-threshold  $\sigma_{np \rightarrow pp\pi^-}$  cross section. However, with increasing energy, the prediction underestimates the data more and more where the main discrepancy is due to the description of the cross section  $\sigma_{11}$ . The new data might provide also an interesting testing ground for calculations in the framework of chiral perturbation theory [22].

## 7 Acknowledgements

We express our gratitude to C. Lechanoine-Leluc, D. Rapin and the DPNC of the University of Geneva for providing us the scintillators for the TOF wall and the associated electronics.

We thank M. Laub and J. Zicha for their help with the construction and the setup of the experiment.

We acknowledge the excellent cooperation with the staff of PSI during the installation and running of the experiment and the analysis as well.

We appreciate the contribution of G. Braun, R. Fastner, H. Fischer and J. Urban.

We especially thank C. Hanhart for the stimulating discussions and for providing us the numerical values of the calculations in the Jülich model.

This work has been funded by the German Bundesministerium für Bildung und Forschung under the contract No. 06FR845.

## References

1. H. O. Meyer et al., Phys. Rev. Lett. **65**, 2846 (1990)
2. D. S. Koltun and A. Reitan, Phys. Rev. **141**, 1413 (1966)
3. C. J. Horowitz, Phys. Rev. **C48**, 2920 (1993)
4. G. A. Miller and P. U. Sauer, Phys. Rev. **C44**, R1725 (1991)
5. J. A. Niskanen, Phys. Lett. **B289**, 227 (1992); Phys. Rev. **C49**, 1285 (1994)
6. T.-S. H. Lee and D. O. Riska, Phys. Rev. Lett. **70**, 2237 (1993)
7. E. Hernández and E. Oset, Phys. Lett. **B350**, 158 (1995)
8. C. Hanhart et al., Phys. Lett. **B358**, 21 (1995)
9. J. Haidenbauer, C. Hanhart and J. Speth, Acta Phys. Pol. **B27**, 2893 (1996)
10. C. Hanhart et al., Phys. Lett. **B444**, 25 (1998)
11. C. Hanhart et al., Phys. Rev. **C61**, 064008 (2000)
12. Y. Maeda,  $\pi N$  newsletters **13**, 326 (1997)
13. K. Tamura, Nuclear Physics at Storage Rings, AIP conference proceedings **512**, 117 (1999)
14. B.-Y. Park et al., Phys. Rev. **C53**, 1519 (1996)

15. T. D. Cohen et al., Phys. Rev. **C53**, 2661 (1996)
16. U. van Kolck, G. A. Miller and D. O. Riska, Phys. Lett. **B388**, 679 (1996)
17. T. Sato et al., Phys. Rev. **C56**, 1246 (1997)
18. C. Hanhart et al., Phys. Lett. **B424**, 8 (1998)
19. E. Gedalin, A. Moalem and L. Razsdolskaya, Phys. Rev. **C60**, 031001 (R) (1999)
20. S. Ando, T. Park and D. Min, "Threshold  $p p \rightarrow p p \pi^0$  up to one-loop accuracy," nucl-th/0003004
21. V. Dmitrašinović, K. Kubodera, F. Myhrer and T. Sato, Phys. Lett. **B465** 43 (1999)
22. C. Hanhart, U. van Kolck and G. A. Miller, Phys. Rev. Lett. **85** 2905 (2000)
23. A. H. Rosenfeld, Phys. Rev. **96**, 139 (1954)
24. A. Bondar et al., Phys. Lett **B356**, 8 (1995)
25. J. G. Hardie et al., Phys. Rev. **C56**, 20 (1997)
26. G. Fäldt and C. Wilkin, Phys. Rev. **C56**, 2067 (1997).
27. R. W. Flammang et al., Phys. Rev. **C 58**, 916 (1998).
28. R. Handler, Phys. Rev. **138**, 1230 (1965)
29. J. G. Rushbrooke et al., Nuovo Cimento **33**, 1509 (1964)
30. V. P. Dzhelepov et al., Sov. Phys. JETP **23**, 993 (1966)
31. M. Kleinschmidt et al., Z. Phys. **A298**, 253 (1980)
32. G. Rappenecker et al., Nucl. Phys. **A590**, 763 (1995)
33. W. Thomas et al., Phys. Rev. **D24**, 1736 (1981)
34. L. G. Dakhno et al., Phys. Lett. **B114**, 409 (1982)
35. T. Tsuboyama et al., Nucl. Phys. **A486**, 669 (1988)
36. B. J. VerWest and R. A. Arndt, Phys. Rev. **C25**, 1979 (1982)
37. J. Bystricky et al., J. Physique **48**, 1901 (1987)
38. Yu. M. Kazarinov and Yu. N. Simonov, Sov. Jour. Nucl. Phys. **4**, 100 (1967)
39. A. Bannwarth et al., Nucl. Phys. **A567**, 761 (1994)
40. M. G. Bachman et al., Phys. Rev. **C52**, 495 (1995)
41. C. Hanhart, Dissertation, University of Bonn (1997)
42. Y. Terrien et al., Phys. Lett. **B294**, 40 (1992)
43. F. Duncan et al., Phys. Rev. Lett. **80**, 4390 (1998)
44. H. Hahn et al., Phys. Rev. Lett. **82**, 2258 (1999)
45. H. Lacker, Dissertation, University of Freiburg (2000)
46. J. Arnold et al., Nucl. Instr. & Meth. **A386**, 211 (1997)
47. R. Binz et al., Phys. Lett. **B231**, 323 (1989)
48. Ch. Brönnimann, M. Daum and J. Löffler, Nucl. Instr. & Meth. **A343**, 331 (1994)
49. J. Arnold et al., Eur. Phys. J. **A2**, 411 (1998)
50. P.D. Barnes et al. Nucl. Phys. **A526**, 575 (1991)
51. A. Ahmidouch et al., Nucl. Instr. & Meth. **A326**, 538 (1993)
52. A. Ahmidouch et al., Eur. Phys. J. **C2**, 627 (1998)
53. H.-J. Urban, FPF 244 B, User's Manual, University of Freiburg, Germany, Rev.1: Dec. 1994.
54. N. Hamann et al., Nucl. Instr. & Meth. **A346**, 57 (1994)
55. A. G. Frodesen, O. Skeggstad and H. Tøfte, *Probability and Statistics in Particle Physics*, chapter 10.8, Universitetsforlaget (1979)
56. GEANT 3.21, Detector Description and Simulation Tool, CERN Program Library Long Writeup (1993)
57. K. M. Watson, Phys. Rev. **88**, 1163 (1952)
58. O. Dumbrajs et al., Nucl. Phys. **B216**, 277 (1983)
59. M. G. Bachman, Dissertation, University of Texas (1993)
60. J. Zlomanczuk et al., The Svedberg Laboratory (TSL) and Department of Radiation Sciences at Uppsala University, TSL/ISV-98-0196, (1998)
61. S. Stanislaus et al., Phys. Rev **C44**, 2287 (1991)
62. A. F. Dunaitsev and Yu. D. Prokoshkin, Sov. Phys. JETP **9**, 1179 (1959)
63. R. J. Cence et al., Phys. Rev. **131**, 2713 (1963)
64. H. O. Meyer et al., Phys. Rev. Lett. **83** (1999) 5439
65. R. A. Arndt et al., Phys. Rev. **D45**, 3995 (1992); actual solution 2000
66. V. G. J. Stoks et al., Phys. Rev. **C48**, 792 (1993)
67. C. Lechanoine-Leluc, private communications (2001)
68. J. Franz, E. Rössle, H. Schmitt and L. Schmitt, Physica Scripta **T87**, 14 (2000); L. Schmitt, private communication (2000)
69. W. Hürster, Dissertation, University of Freiburg (1979)
70. G. B. Yodh, Phys. Rev. **98**, 1330 (1955)
71. A. Abdivaliev et al., Nucl. Phys. **B99**, 445 (1975)
72. C. Hanhart, private communication (2001)